ACS APPLIED MATERIALS & INTERFACES

www.acsami.org

Research Article

Structural and Electrochemical Properties of Type VIII $Ba_8Ga_{16-\delta}Sn_{30+\delta}$ Clathrate ($\delta \approx 1$) during Lithiation

Andrew Dopilka, Amanda Childs, Alexander Ovchinnikov, Ran Zhao, Svilen Bobev, Xihong Peng, and Candace K. Chan*

Cite This: *ACS Appl. Mater. Interfaces* 2021, 13, 42564–42578

Read Online

ACCESS | Metrics & More | Article Recommendations | Supporting Information

ABSTRACT: Clathrates of the tetrel (Tt = Si, Ge, Sn) elements are host–guest structures that can undergo Li alloying reactions with high capacities. However, little is known about how the cage structure affects the phase transformations that take place during lithiation. To further this understanding, the structural changes of the type VIII clathrate $Ba_8Ga_{16-\delta}Sn_{30+\delta}$ ($\delta \approx 1$) during lithiation are investigated and compared to those in β-Sn with *ex situ* X-ray total scattering measurements and pair distribution function (PDF) analysis. The results show that the type VIII clathrate undergoes an alloying reaction to form Li-rich amorphous phases ($Li_xBa_{0.17}Ga_{0.33}Sn_{0.67}$, x = 2–3) with local structures similar to those in the crystalline binary Li–Sn phases that form during the lithiation of β-Sn. As a result of the amorphous phase transition, the type VIII clathrate reacts at a lower voltage (0.25 V *vs* Li/Li^+) compared to β-Sn (0.45 V) and goes through a solid-solution reaction after the initial conversion of the crystalline clathrate phase. Cycling experiments suggest that the amorphous phase persists after the first lithiation and results in considerably better cycling than in β-Sn. Density functional theory (DFT) calculations suggest that topotactic Li insertion into the clathrate lattice is not favorable due to the high energy of the Li sites, which is consistent with the experimentally observed amorphous phase transformation. The local structure in the clathrate featuring Ba atoms surrounded by a cage of Ga and Sn atoms is hypothesized to kinetically circumvent the formation of Li–Sn or Li–Ga crystalline phases, which results in better cycling and a lower reaction voltage. Based on the improved electrochemical performance, clathrates could act as tunable precursors to form amorphous Li alloying phases with novel electrochemical properties.

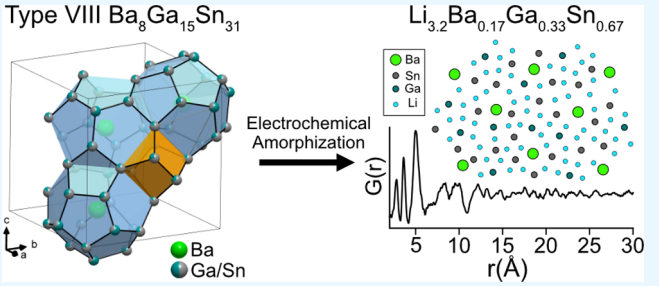

KEYWORDS: *clathrate, amorphous, pair distribution function, density functional theory, lithium, energy storage*

1. INTRODUCTION

Tetrel (Tt = Si, Ge, Sn) clathrates are host–guest materials with the potential for unique properties. While previously associated predominately with their thermoelectric,[1,2] superconducting,[3,4] and optical properties,[5−7] the rich structural and compositional space of clathrates[1] provides wide opportunities for tuning desirable characteristics for their application as next-generation anodes in Li-ion batteries. In tetrel clathrates, a cage framework of covalently bonded Tt elements encapsulates alkali and alkaline earth metal guest atoms. Clathrates can form in various crystal structures with defects such as guest atom vacancies/substitutions and framework vacancies/substitutions,[8] leading to a wide design space. In recent years, our group and others have investigated the electrochemical properties of several clathrates comprising silicon[9−16] and germanium[17−19] frameworks.

We recently used X-ray pair distribution function (PDF) analysis to evaluate the local and long-range structure of the intermediates that form during room-temperature lithiation of Ba_8Ge_{43} and $Ba_8Al_{16}Ge_{30}$ clathrates, which both adopt the type I structure but contain vacancies or Al atoms, respectively, on the Ge framework.[19] The PDF analysis showed that the lithiation of the clathrates proceeded through amorphous phase transformations, different from those in diamond cubic Ge (α-Ge), which often progress through crystalline phases.[20] We hypothesized that during the lithiation process, the Ba atoms act as "pillars" that kinetically prevent long-range ordering of the regions rich in Li–Ge bonding, which results in suppression of crystalline phase formation. In these regions, the amorphous Li–Ge phases showed similar local structuring to Li–Ge crystalline phases of comparable composition, which was supported by the low-temperature amorphous-to-crystalline transformation observed with *in situ* PDF heating studies. Despite the destruction of the crystalline clathrate structure after lithiation, the PDF analysis showed that the cage-like local

Received: April 20, 2021
Accepted: August 4, 2021
Published: September 3, 2021

structure is preserved after delithiation. A consequence of this amorphous phase transformation is that lithium reacts *via* a solid-solution mechanism and at a lower voltage *vs* Li/Li^+ relative to α-Ge, which are both beneficial properties for Li-ion battery anodes.

To further understand how the clathrate structure and composition affect its electrochemical reactivity with Li, herein we investigate the lithiation of the type VIII clathrate, which has a different but closely related structure than the previously investigated Ba−Ge clathrates with type I structure (Figure 1a). Both clathrate structures can be described with the same ideal formula, M_8Tt_{46} (M = guest atom such as Na, Ba, *etc.*), but display different crystal chemistry.[21] The type VIII clathrate crystal structure is described in an $I\bar{4}3m$ space group and is composed of face-sharing distorted dodecahedra (Tt_{20}) filled by M-atoms and smaller voids (Figure 1b).[22,23] This is notably different from the type I structure, which is composed of six larger tetrakaidecahedra (Tt_{24}) and two pentagonal dodecahedra (Tt_{20}) per formula unit.[2] The polyhedra of the type VIII clathrate can be described as a strongly distorted version of the perfect dodecahedra found in the type I structure.[21] Different from the Tt_{20} dodecahedra in type I clathrates, which contain only pentagonal faces, the Tt_{20} distorted dodecahedra in type VIII clathrates contain three, four, and five atom faces, which form six-membered and five-membered rings. In our previous studies, we identified Li migration through hexagonal faces as being associated with much lower-energy barriers compared to migration through pentagonal faces.[24] Therefore, investigating the possibility of topotactic Li insertion through the six-membered rings of the distorted dodecahedra in the type VIII clathrate structure is of interest. In addition, the voids in the type VIII structure could provide a unique access point for Li into the polyhedral network, which has previously not been investigated.

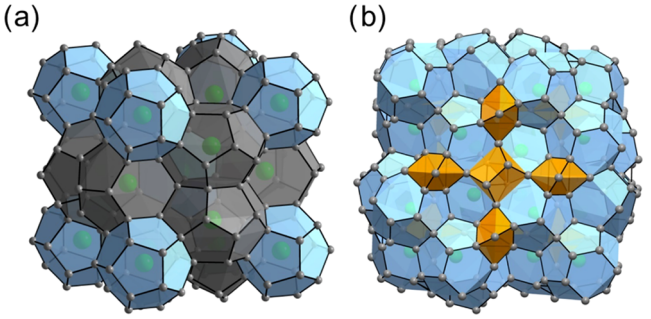

Figure 1. Crystal structures of (a) type I and (b) type VIII clathrates with ideal formulas M_8Tt_{46}. The gray atoms represent the Tt framework atoms and the green atoms represent the M guest atoms. The dodecahedra (Tt_{20}) and distorted dodecahedra are shaded in blue, the tetrakaidecahedra (Tt_{24}) in the type I structure are shaded in gray, and the voids in the type VIII structure are shaded in orange.

Herein, we investigate the properties of type VIII clathrate $Ba_8Ga_{16-\delta}Sn_{30+\delta}$ ($\delta \approx 1$), where a partial substitution of Sn for Ga atoms occurs on all framework sites. In an extension of our previous analysis comparing the lithiation properties in type I clathrate $Ba_8Ge_{43}\square_3$ ($\square$ = vacancy) and $Ba_8Al_{16}Ge_{30}$ with those of α-Ge, herein, we report a comparative study of the

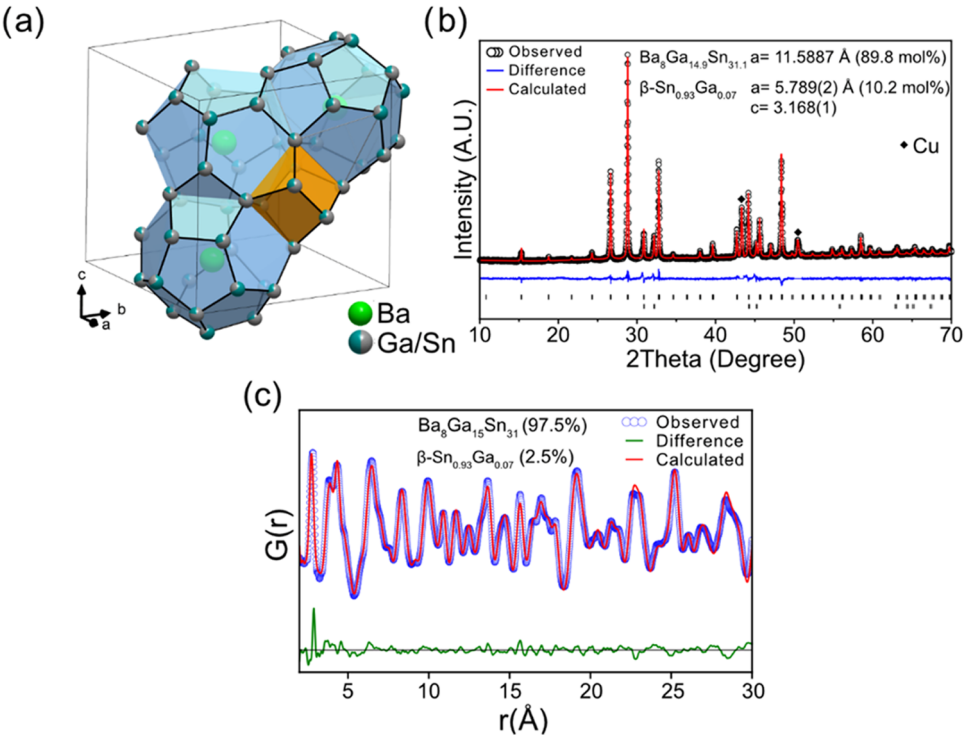

Figure 2. (a) Crystal structure of type VIII $Ba_8Ga_{15}Sn_{31}$ clathrate derived from the single-crystal refinement (Tables S1 and S2). The relative fractions of gray/blue spheres represent the occupancy of Sn/Ga atoms on framework sites, and the green spheres represent the Ba atoms. The distorted dodecahedra are shaded in blue, while the void is shaded in orange. (b) Rietveld refinement of the PXRD pattern of the electrode used in the electrochemical experiments. The lattice and atomic parameters of $Ba_8Ga_{14.9}Sn_{31.1}$ were fixed to that found in the single-crystal refinement. The top set of tick marks corresponds to the $Ba_8Ga_{14.9}Sn_{31.1}$ phase ($I\bar{4}3m$), and the bottom set corresponds to β-$Sn_{0.93}Ga_{0.07}$ ($I4_1/amd$). Refinement residuals: $\chi^2 = 1.58$, $R_p = 0.042$, and $wR_p = 0.057$. (c) PDF refinement ($R_w = 15.1\%$) of pristine $Ba_8Ga_{15}Sn_{31}$ using the structural model derived from the single-crystal refinement (Tables S1 and S2). Phase fractions are in terms of mol %.

https://doi.org/10.1021/acsami.1c07240
ACS Appl. Mater. Interfaces 2021, 13, 42564−42578

lithiation properties of type VIII clathrate with β-Sn. We find that the type VIII clathrate decomposes during the reaction with Li to form a highly lithiated amorphous phase and displays electrochemical properties distinct from those observed during lithiation of the Sn and Ga elemental phases. This is attributed to the assembly of Sn and Ga into the clathrate structure with Ba guest atoms, suggesting the possibility for novel amorphous alloy phases originating from clathrate precursors for anode materials.

2. EXPERIMENTAL METHODS

The clathrate was prepared in a Sn flux using conditions that favor the type VIII over type I clathrate structure as described previously[23] and the composition was confirmed by single-crystal X-ray diffraction (XRD). More details can be found in the Supporting Information. Slurries containing the active material (type VIII clathrate or commercially obtained β-Sn powder), carbon black, and binder were prepared and coated onto the copper foil (see the Supporting Information). These composite electrodes were then lithiated galvanostatically in half-cells with lithium metal and then extracted for *ex situ* measurements. Synchrotron X-ray pair distribution (PDF) measurements were conducted at Diamond Light Source (Didcot, U.K.) at the I15-I dedicated PDF beamline with $\lambda = 0.161669$ Å. The atomic PDF, $G(r)$, as defined by Billinge et al.,[25] was generated from the total scattering data using PDFgetx3 within the xPDF suite software package.[26,27] The first-principles density functional theory (DFT) calculations were performed in a similar manner to our previous work[13,16,18,24] and are described in more detail in the Supporting Information. The Gibbs free-energy change, average lithiation voltage, and formation energy were calculated as described previously.[13,18,24] The climbing image nudged elastic band (NEB) method was used to calculate the Li migration barriers.[28] More detailed descriptions of the synthesis, electrochemical, synchrotron measurements, PDF analysis, and DFT calculations are in the Supporting Information.

3. RESULTS

3.1. Type VIII Ba−Ga−Sn Clathrate Structure. Single-crystal XRD analysis of the products of the flux reaction (see Tables S1 and S2 for refinement and structural details) confirmed that the synthesized materials adopted the type VIII clathrate crystal structure with a refined composition of $Ba_8Ga_{14.9}Sn_{31.1(4)}$; for simplicity, $Ba_8Ga_{15}Sn_{31}$ is used as the composition for the subsequent electrochemical characterization. A close-up view of the crystal structure of $Ba_8Ga_{15}Sn_{31}$ is shown in Figure 2a. Energy-dispersive X-ray spectroscopy (EDS) characterization of the single-crystal particles supports the composition derived from the single-crystal XRD refinement (Figure S1a). Laboratory powder XRD (PXRD) performed on the as-synthesized clathrate powders confirmed that the product mainly consisted of the type VIII clathrate along with other impurities (Figure S1b). To quantify the phase fractions, Rietveld refinement analysis was performed on the PXRD pattern of the electrode (Figure 2b). The diffraction pattern showed reflections corresponding to the type VIII clathrate phase along with a 10.2 mol % phase fraction of β-$Sn_{0.93}Ga_{0.07}$, which likely originates from the residual Sn flux from the synthesis. The presence of Ga substitution in the β-Sn phase was determined based on the lattice parameter, which matched well with a previous report ($a = 5.784$ Å, $c = 3.168$ Å for β-$Sn_{0.93}Ga_{0.07}$).[29] Synchrotron PDF analysis was also used to quantify the amount of β-phase impurity in the clathrate sample. The PDF refinement of the pristine clathrate (Figure 2c and Table S3) showed that the PDF fit the structural model derived from the single-crystal structural refinements presented herein (Tables S1 and S2) with a fraction of β-$Sn_{0.93}Ga_{0.07}$ (2.5 mol %). The Rietveld and PDF refinements give different values for the phase fraction of β-$Sn_{0.93}Ga_{0.07}$ in the sample, which could originate from particle size effects from loading the powder into the capillary for PDF measurements. The PXRD pattern of the electrode is expected to be more representative of the phases present during electrochemical lithiation as the powder was well mixed in a slurry before casting the electrode.

3.2. Electrochemical Lithiation. To investigate the structures that form upon lithiation, the type VIII clathrate and β-Sn electrodes were electrochemically lithiated with similar amounts of Li and then subjected to total scattering experiments to obtain structure function and PDF plots. Scanning electron microscopy (SEM) imaging of the electrodes prior to lithiation (Figure S2) showed that the type VIII clathrate was composed of irregularly shaped particles 2−20 μm in size with small spherical β-$Sn_{0.93}Ga_{0.07}$ impurities, while the β-Sn electrode prepared for comparison was composed of 1−5 μm spherical particles.

The voltage profiles and corresponding dQ/dE plots for the first lithiation of β-Sn and $Ba_8Ga_{15}Sn_{31}$ are presented in Figure 3, with teal, orange, green, and blue points representing the compositions at which samples were collected for total scattering measurements. The voltages and capacities of the cells at these points in the lithiation process are presented in Table S4. Note that the number of Li added to each electrode is normalized to the amount of Sn or (Ga + Sn) atoms in each starting compound.

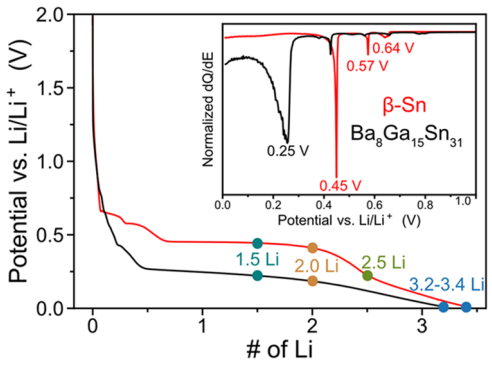

Figure 3. Voltage profile and corresponding dQ/dE plot of the lithiation of $Ba_8Ga_{15}Sn_{31}$ (black) and β-Sn (red) at 12.5 and 25 mA/g, respectively, with a voltage cutoff of 10 mV *vs* Li/Li$^+$. The circles represent the points where cells were disassembled for *ex situ* total scattering measurements. The # of Li is normalized to the amount of nonalkali/alkaline earth metal atoms.

The room-temperature voltage profile of β-Sn is characterized by three voltage plateaus and then a sloped curve until reaching a cutoff voltage of 10 mV *vs* Li/Li$^+$. The plateaus at 0.64 and 0.57 V *vs* Li/Li$^+$ (represented as peaks in the dQ/dE plot) have been assigned to the formation of Li_2Sn_5[30] and LiSn,[31] respectively.[32−37] The plateau at 0.45 V has been previously assigned to an amorphous transition on the basis of *in situ* XRD analysis,[33,35] while an *in operando* NMR study of the lithiation of Sn nanoparticles recently assigned this plateau to the conversion of LiSn to Li_7Sn_3 and then $Li_{13}Sn_5$.[36] After the plateau at 0.45 V, the voltage profile is more sloped and reaches a final composition of 3.4 Li per Sn, which contains less Li than the theoretical maximum based on the most Li-rich

https://doi.org/10.1021/acsami.1c07240
ACS Appl. Mater. Interfaces 2021, 13, 42564−42578

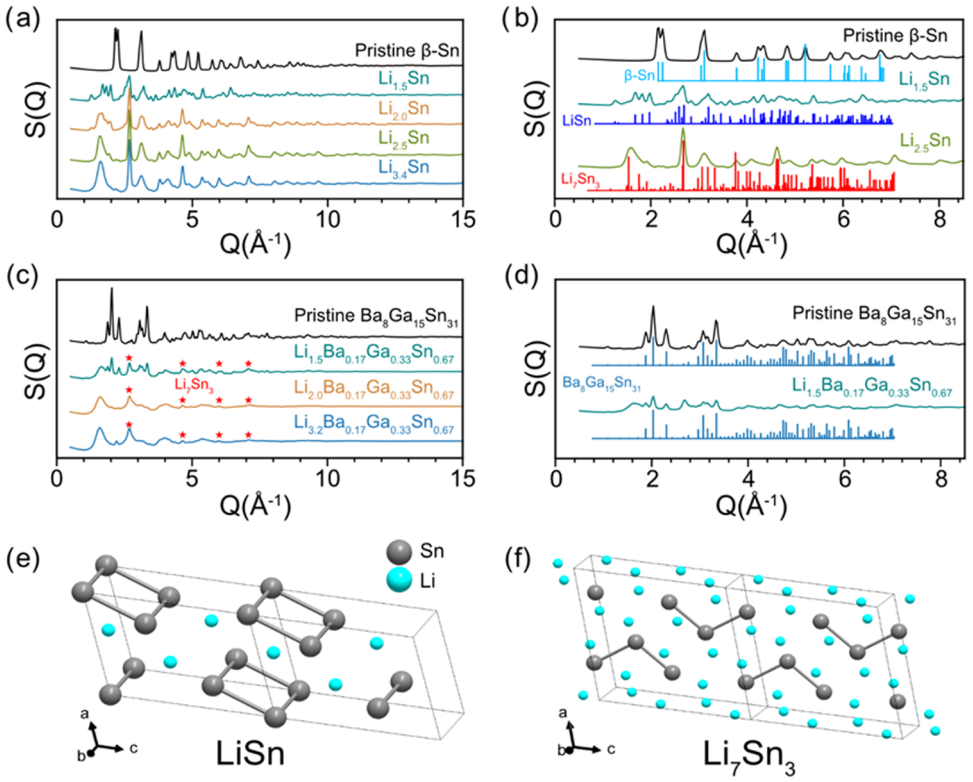

Figure 4. (a) Structure function plots for pristine β-Sn and lithiated β-Sn electrodes. (b) Comparison of structure function plots for β-Sn, $Li_{1.5}Sn$, and $Li_{2.5}Sn$ with calculated reference patterns for β-Sn, LiSn, and Li_7Sn_3. (c) Structure function plots for pristine $Ba_8Ga_{15}Sn_{31}$ and lithiated clathrate electrodes. (d) Comparison of structure function plots for pristine clathrate and $Li_{1.5}Ba_{0.17}Ga_{0.33}Sn_{0.67}$ with reference pattern for $Ba_8Ga_{15}Sn_{31}$ (from single-crystal refinement; see Tables S1 and S2). Crystal structures of intermediate phases identified in the lithiation of β-Sn: (e) LiSn (data taken from ref 31) and (f) Li_7Sn_3 (data taken from ref 41).

compound (previously $Li_{22}Sn_5$ but later identified as $Li_{17}Sn_4$[38]) from the Li−Sn phase diagram but is similar to previous experimental reports.[32,37] It has been proposed that disordered $Li_{17}Sn_4$ forms in this sloped voltage region[39,40] by X-ray diffraction analysis, as well as Li_7Sn_2 *via* NMR measurements.[36]

The lithiation of the type VIII clathrate is characterized by a voltage plateau starting at 0.25 V (seen as a peak in the dQ/dE plot) and then a sloping profile. We assign the process occurring at 0.25 V to the lithiation of the type VIII clathrate phase. The sample reacts with around 3.2 Li per (Ga + Sn) atom, which suggests that the clathrate is being converted into a phase containing high Li content. We note that this composition is an overestimate due to the presence of β-$Sn_{0.93}Ga_{0.07}$ as an impurity (which is identified by the small peaks from 0.40 to 0.64 V in the dQ/dE plot that match those in the β-Sn electrode). Additionally, there is likely the formation of a solid electrolyte interphase (SEI) due to electrolyte reduction in the first lithiation; both of these processes are expected to consume lithium.

3.3. Structure Function Patterns. Structure function patterns, $S(Q)$, derived from the total scattering patterns for the β-Sn and $Ba_8Ga_{15}Sn_{31}$ electrodes before and after lithiation are presented in Figure 4a,c, respectively. The structure function plots allow for the observation of Bragg peaks at low scattering angles and to tentatively identify the major crystalline phases present in the sample by comparison with calculated reference patterns. To aid comparison, the plots for the lithiated electrodes are labeled at the compositions indicated by the points in Figure 3, *i.e.*, Li_xSn (x = 1.5, 2.0, 2.5, 3.4) for the lithiated β-Sn compositions and $Li_xBa_{0.17}Ga_{0.33}Sn_{0.67}$ (x = 1.5, 2.0, 3.2) for the lithiated clathrate compositions (Li amounts are normalized to the amount of nonalkali/alkaline earth metal atoms). Figure 4b,d shows the structure function patterns with the calculated reference patterns of the identified phases. For the β-Sn electrodes (Figure 4a), reflections corresponding to β-Sn disappear and a series of other reflections appear as the Li composition increases during lithiation. At a composition of $Li_{1.5}Sn$, reflections corresponding to LiSn ($P2/m$)[31] are present, as seen by the comparison of the calculated reference pattern with the structure function (Figure 4b). In the $Li_{2.0}Sn$ pattern, the reflections corresponding to LiSn ($P2/m$)[31] decrease in favor of another set of reflections that are assigned to Li_7Sn_3 ($P2_1/m$),[41] which suggests that a two-phase reaction is occurring in this part of the lithiation process. Crystal structures of LiSn and Li_7Sn_3 are shown in Figure 4e,f and demonstrate how the Sn square units in LiSn are broken up to form Sn trimers in the Li_7Sn_3 phase. At a composition of $Li_{2.5}Sn$, the sample appears to be mainly composed of Li_7Sn_3 based on the comparison to the calculated pattern (Figure 4b). For the electrode with composition $Li_{3.4}Sn$, the pattern is similar to that for $Li_{2.5}Sn$, suggesting that Li_7Sn_3 is still present but with slight changes to some of the intensities of the reflections. Overall, the structure function patterns confirm that the lithiation of β-Sn proceeds through crystalline phase transformations.

For the structure function patterns of the type VIII clathrate (Figure 4c), the pristine (unlithiated) sample shows reflections matching the calculated pattern for the type VIII $Ba_8Ga_{15}Sn_{31}$ structure obtained from the single-crystal refinement (Figure 4d), consistent with the lab PXRD results. Lithiation to a

https://doi.org/10.1021/acsami.1c07240
ACS Appl. Mater. Interfaces 2021, 13, 42564−42578

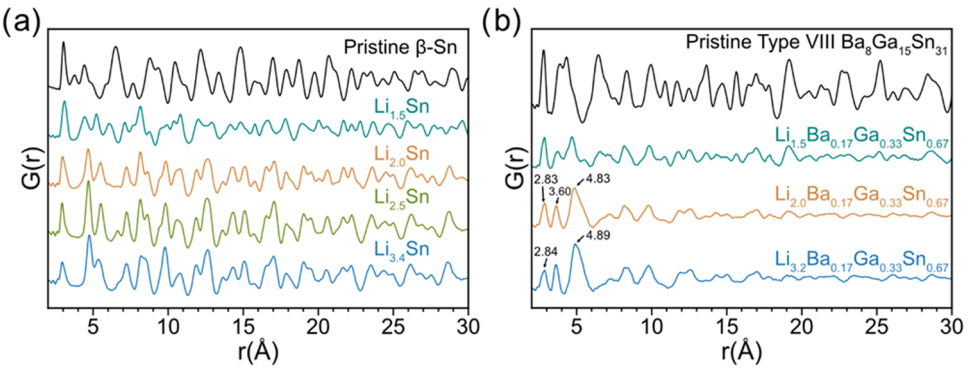

Figure 5. (a) *Ex situ* X-ray PDFs for pristine β-Sn, $Li_{1.5}Sn$, $Li_{2.0}Sn$, $Li_{2.5}Sn$, and $Li_{3.4}Sn$. (b) *Ex situ* X-ray PDFs for pristine $Ba_8Ga_{15}Sn_{31}$, $Li_{1.5}Ba_{0.17}Ga_{0.33}Sn_{0.67}$, $Li_{2.0}Ba_{0.17}Ga_{0.33}Sn_{0.67}$, and $Li_{3.2}Ba_{0.17}Ga_{0.33}Sn_{0.67}$.

composition of $Li_{1.5}Ba_{0.17}Ga_{0.33}Sn_{0.67}$ resulted in a decrease in the intensity of reflections corresponding to $Ba_8Ga_{15}Sn_{31}$ and the emergence of several broad peaks. No other significant reflections are present, suggesting that the broad peaks originate from an amorphous phase. At a composition of $Li_{2.0}Ba_{0.17}Ga_{0.33}Sn_{0.67}$, the pattern only displays the broad reflections associated with the amorphous phase and there are no significant reflections past 5 $Å^{-1}$, suggesting that the type VIII clathrate has been fully converted into the amorphous phase. Low-intensity reflections (Figure 4c, marked as red stars) are observed that match those in the calculated pattern for Li_7Sn_3; the presence of these reflections is attributed to the lithiation of the β-$Sn_{0.93}Ga_{0.07}$ impurity phase to form Li_7Sn_3. For $Li_{3.2}Ba_{0.17}Ga_{0.33}Sn_{0.67}$, the structure function pattern is similar to the pattern for $Li_{2.0}Ba_{0.17}Ga_{0.33}Sn_{0.67}$ but with slightly shifted intensities for the broad peaks. Analysis of the structure function patterns of the intermediates formed during reaction of Li with $Ba_8Ga_{15}Sn_{31}$ suggests that lithiation proceeds through the conversion of the clathrate phase to an amorphous phase.

3.4. Pair Distribution Function Analysis. By taking a Fourier transform of the reduced structure functions, the total scattering data can be analyzed in real space and allows for the observation of local structural changes through the pair distribution function (PDF).[25] The PDF plot provides a weighted histogram of all atom−atom distances within a material and has been used to great effect to understand electrochemical alloying reactions.[19,20,42−45] The calculated PDF patterns for Li−Sn crystalline phases and $Ba_8Ga_{15}Sn_{31}$ discussed herein are presented in Figures S3 and S4, respectively.

Ex situ PDF plots for the lithiated β-Sn and the type VIII clathrate electrodes are presented in Figure 5. The PDF refinement for the pristine β-Sn sample fit the structural model well, suggesting phase-pure starting material (Figure S5). The PDFs of the β-Sn after lithiation were refined (Figure S6 and parameters in Table S5) from 2 to 15 Å to LiSn, Li_7Sn_3, and Li_7Sn_2 based on the expected reaction products from the structure function plots (Figure 4a,b) and from previously reported assignments.[32] The PDF for the electrode lithiated to a composition of $Li_{1.5}Sn$ was fit to LiSn and Li_7Sn_3, the expected products at this composition, and resulted in a relatively good fit (R_w = 15.9%) with phase fractions of 70 mol % LiSn and 30 mol % Li_7Sn_3 (Figure S6a). For the $Li_{2.0}Sn$ sample, the PDF was fit to 82 mol % Li_7Sn_3 and 18 mol % LiSn with an R_w of 11.5% (Figure S6b). The $Li_{2.5}Sn$ pattern was fit well by considering Li_7Sn_3 as the sole phase (R_w = 13.9%; Figure S6c), while the $Li_{3.4}Sn$ PDF was fit well to a mixture of 53 mol % Li_7Sn_3 and 47 mol % Li_7Sn_2 (R_w = 19.9%; Figure S6d). Interestingly, when the fit range was increased to 30 Å, the fit was worse for PDFs containing Li_7Sn_3 (see Figure S6e), with the high-*r* correlations from 20 to 30 Å not captured well by the Li_7Sn_3 model. Another study showed that Li_7Sn_3 synthesized *via* ball-milling and annealing showed a good fit of the PDF to the Li_7Sn_3 structure from 2 to 30 Å,[43] suggesting that the deviation from the Li_7Sn_3 structural model observed in our results (Figure S6e) might be related to the electrochemical formation of Li_7Sn_3 at room temperature. Overall, the PDF analysis shows that the lithiation of β-Sn proceeds through crystalline phase transformations in which the Sn clusters in LiSn (Figure 4e) are transformed into smaller units until Sn dumbbells/trimers and single Sn atoms surrounded by Li atoms (as seen in Li_7Sn_3 and Li_7Sn_2; see Figures 4f and S6f, respectively) are the dominant features present at the end of lithiation.

In the case of the clathrate samples, since the intensity of X-ray PDF correlations is dependent on the atomic number of the elements, the Sn atomic correlations are expected to contribute the most to the observed PDF patterns. The higher contribution of the Sn−Sn and Sn−Ga correlations to the total PDF pattern for $Ba_8Ga_{15}Sn_{31}$ can be readily seen in the calculated pattern in Figure S4. Inspection of this PDF shows that the first, second, and third correlations in the total PDF pattern correspond to direct Sn/Ga−Sn/Ga bonding, Ba−Sn/Ga distances, and next-nearest neighbor Sn/Ga distances, respectively. The PDF results for the lithiation of the type VIII $Ba_8Ga_{15}Sn_{31}$ (Figure 5b) show that lithiation of the clathrate results in decreased intensities and significant shifts in the correlations, which is indicative of phase transformations. Refinement of the PDF from $Li_{1.5}Ba_{0.17}Ga_{0.33}Sn_{0.67}$ showed that correlations corresponding to the pristine type VIII clathrate are still present, but the refinement could not capture all of the correlations at high-*r* values (10−30 Å) (Figure S7a). Adding Li_7Sn_3 to the refinement as a second phase results in a better fit with 30 mol % clathrate and 70 mol % Li_7Sn_3 (Figure S7b and Table S6). We attribute the presence of Li_7Sn_3 to originate from the lithiation of the β-$Sn_{0.93}Ga_{0.07}$ impurity in the clathrate sample. Li_7Sn_3 was chosen as the second phase for the refinement because it is the expected product from the lithiation of β-Sn at the voltage of this particular electrode (0.17 V); furthermore, the Bragg peaks in the structure function pattern of this sample showed reflections from both the clathrate and Li_7Sn_3 structures (Figure 4c). After fitting the PDF pattern to the clathrate and Li_7Sn_3 phases, three peaks

https://doi.org/10.1021/acsami.1c07240
ACS Appl. Mater. Interfaces 2021, 13, 42564−42578

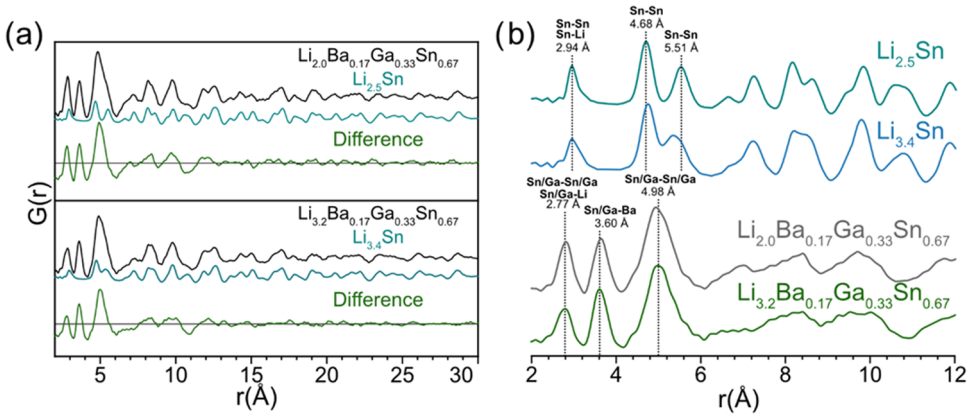

Figure 6. (a) Difference curves resulting from the subtraction of the Li−Sn PDF (crystalline impurity phase) from the PDF of the amorphous phase formed during lithiation of the clathrate. (b) Comparison of the lithiated PDFs for β-Sn and the type VIII clathrate with the indicated compositions. From the refinements, the electrode with composition $Li_{2.5}Sn$ was determined to contain Li_7Sn_3, while the electrode with composition $Li_{3.4}Sn$ contained a mixture of Li_7Sn_3 and Li_7Sn_2.

appear in the difference plot at r values of 2.88, 3.60, and 4.70 Å (Figure S7b). We attribute the origins of these correlations to the lithiated amorphous phase that forms when lithium reacts with the clathrate. This result is similar to our previous PDF analysis of type I clathrate Ba_8Ge_{43} after lithiation, where a similar treatment of the refinement revealed an amorphous phase with three peaks at low-r values in the difference plot.[19] Based on the similar result and absence of other Bragg peaks appearing in the structure function pattern (Figure 4c), we attribute the peaks in the difference plot to an amorphous Li−Ba−Ga−Sn phase that coexists with the pristine (unlithiated) clathrate phase at this stage of the lithiation process.

Further lithiation of the type VIII clathrate to a composition of $Li_{2.0}Ba_{0.17}Ga_{0.33}Sn_{0.67}$ resulted in further decreases in the intensity of the high-r correlations ($10 < r < 30$ Å), suggesting the complete conversion of the crystalline $Ba_8Ga_{15}Sn_{31}$ by this point, consistent with the structure function plots (Figure 4c). At low-r values ($2 < r < 5$ Å), three main correlations are present at 2.83, 3.60, and 4.83 Å. These correlations are at similar distances to those attributed to the amorphous phase in the PDF for $Li_{1.5}Ba_{0.17}Ga_{0.33}Sn_{0.67}$ (Figure S7b), suggesting that the amorphous phase continues to grow at the expense of the pristine clathrate phase. The low intensity of correlations past 15 Å indicates the absence of long-range order in the sample, consistent with the broad peaks in the structure function pattern (Figure 4c). Further lithiation to $Li_{3.2}Ba_{0.17}Ga_{0.33}Sn_{0.67}$ shows a similar PDF pattern as that for $Li_{2.0}Ba_{0.17}Ga_{0.33}Sn_{0.67}$, but the first correlation at 2.84 Å has a lower intensity relative to the correlation at 4.89 Å, an indication that Sn/Ga−Sn/Ga bonds are being broken to form more Sn/Ga single atoms. Furthermore, the presence of low-intensity correlations from 15 to 30 Å in both PDF patterns suggests the presence of a small amount of crystalline phase; we attribute this to possible Li−Sn crystalline phases formed from the reaction of the β-$Sn_{0.93}Ga_{0.07}$ impurity present in the clathrate starting material as described previously (Figure 2b).

From these results, it appears that the Li−Sn crystalline phases that form upon lithiation of the β-$Sn_{0.93}Ga_{0.07}$ impurity contribute substantially to the PDF of the lithiated clathrate electrode, especially at high-r values. To better elucidate the local structure of the amorphous phases formed upon lithiation of the clathrate, the contribution of the residual crystalline Li−Sn compounds was removed by subtracting the appropriate experimental Li_xSn PDF from the PDFs of the lithiated clathrates. The results of this process are shown in Figure 6a. For the PDF of $Li_{2.0}Ba_{0.17}Ga_{0.33}Sn_{0.67}$, the subtraction was performed using the PDF taken from the $Li_{2.5}Sn$ electrode because both cells were lithiated to a similar voltage (Table S4). The experimental PDF was scaled to fit over the high-r correlations and then subtracted from the clathrate PDF. The correlations from the experimental $Li_{2.5}Sn$ PDF, which was refined to 100% Li_7Sn_3 (Figure S6c), matched the high-r correlations of the lithiated type VIII clathrate well, as seen by the low intensity in the difference curve from $15 < r < 30$ Å (Figure 6a). Based on the good fit, we expect that the small amount of Ga alloying (7%) into the Sn phase (Figure 2b) did not significantly affect the structures of the lithiated phases compared to those of the pure Li−Sn compositions. A similar process was conducted for the PDF of $Li_{3.2}Ba_{0.17}Ga_{0.33}Sn_{0.67}$ but using subtraction of the PDF from $Li_{3.4}Sn$. Attempts were made to refine the experimental patterns of $Li_{2.0}Ba_{0.17}Ga_{0.33}Sn_{0.67}$ and $Li_{3.2}Ba_{0.17}Ga_{0.33}Sn_{0.67}$ to the structure of Li_7Sn_3 (Figure S7c,d). The results showed a similar difference plot from 2 to 10 Å as those shown in Figure 6a, but the high-r (20−30 Å) correlations were not fit as well, consistent with the poor fit to Li_7Sn_3 observed in the refinement of the $Li_{2.5}Sn$ PDF from 20 to 30 Å (Figure S6e). The contributions from the impurity Li−Sn crystalline phases were dominant in the PDF above 6 Å, and by subtracting them from the clathrate PDFs, it gives a clearer picture of the features originating from the lithiated amorphous phase formed upon the reaction of lithium with the clathrate.

In Figure 6b, the PDF patterns for the β-Sn and type VIII clathrate samples after lithiation are compared. The lowest r values are at 2.94 and 2.77 Å, respectively. In many binary Li−Sn compounds, the first correlation in the PDF is a combination of direct Sn−Sn bonding and Li−Sn correlations (Figure S3). The Sn−Sn bond lengths in Li_7Sn_3 and Li_7Sn_2 are 3.00 and 2.95 Å, respectively, which matches the correlation at 2.94 Å and is slightly shorter than the Sn−Sn bond length in β-Sn of 3.11 Å. In comparison, the first correlation seen in the lithiated clathrate with a composition of $Li_{3.2}Ba_{0.17}Ga_{0.33}Sn_{0.67}$ (2.77 Å) is much shorter than the first correlation distances in β-Sn, Li_7Sn_3, and Li_7Sn_2 while slightly larger than the Sn−Ga bond length in the pristine type VIII clathrate structure (2.642−2.764 Å).[23] This suggests that the Ga atoms are

https://doi.org/10.1021/acsami.1c07240
ACS Appl. Mater. Interfaces 2021, 13, 42564−42578

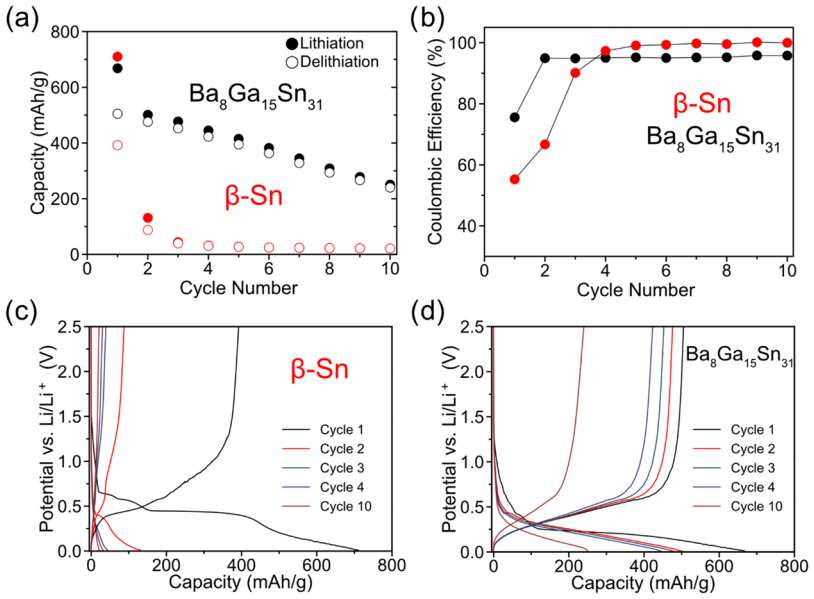

Figure 7. (a) Capacity and (b) Coulombic efficiency *vs* cycle number for β-Sn and type VIII $Ba_8Ga_{15}Sn_{31}$ clathrate electrodes in half-cells cycled at 12.5 mA/g with a voltage range of 0.01−2.5 V *vs* Li/Li^+. Voltage profiles for (c) β-Sn and (d) type VIII $Ba_8Ga_{15}Sn_{31}$ clathrates.

participating in bonding with Sn in the amorphous lithiated phase and thus results in a lower average bond length when compared to pure Sn−Sn bonding. The next correlation occurs at 3.60 Å for the clathrate-derived lithiated phases, which is similar to the Ba−Ga/Sn distances in the pristine clathrate phase (3.632−3.852 Å).[23] The absence of this peak in the PDFs of the Li−Sn reference compounds (Figure S3), as well as the lithiated β-Sn samples, confirms that it is associated with Ba−Ga/Sn correlations. This Ba correlation is also notably similar to the Ba−Ge distance (3.44 Å) observed previously in the PDFs of amorphous Li−Ba−Ge phases formed after lithiation of type I Ba−Ge clathrates.[19] The correlations at 4.68 and 5.51 Å in the $Li_{2.5}Sn$ PDF are associated with two different next-nearest neighbor Sn−Sn correlations in the Li_7Sn_3 phase (Figure S3b). In the clathrate sample, a single correlation is centered at 4.98 Å. The splitting of this peak into two correlations is a consequence of the parallel alignment of two different next-nearest-neighbor distances of Sn−Sn units (Sn trimers in the case of Li_7Sn_3; see Figures 4f and S8), while it becomes a single peak as the amount of isolated Sn atoms increases (as in Li_7Sn_2; see Figures S3c and S6f). The peak at 4.98 Å for the clathrate sample is expected to correspond to a similar type of the next-nearest-neighbor correlation; however, the peak is not split, which could be due to a disorder between Sn/Ga−Sn/Ga units in the amorphous phase or the presence of more isolated single atoms. We note that this single peak at 4.98 Å is a feature similar to that observed in the PDFs of amorphous lithiated Ba_8Ge_{43}[19] and in lithiated nanoparticles of amorphous Ge and has been attributed to the absence of parallel alignment of adjacent dumbells.[43] Another notable feature in the PDFs for both β-Sn and the clathrate materials is the decrease in intensity of the first correlation (2.7−2.9 Å) relative to the correlations from 4.7 to 5.2 Å as the Li content increases. This behavior is indicative of a breaking of direct Sn/Ga bonds resulting in more isolated Sn/Ga atoms surrounded by Li, which manifests as a single peak around 5 Å. This is seen in the PDF of $Li_{3.4}Sn$ (Figure 5a) where instead of completely two split peaks (as seen in $Li_{2.5}Sn$ at 4.68 and 5.51 Å), these correlations are starting to merge, which is an indication that the Sn trimers are being broken up in favor of single Sn atoms. Since a similar trend is observed for the clathrate sample, we suspect that Sn/Ga−Sn/Ga bonds are being broken in an analogous manner albeit *via* a more disordered arrangement.

Finally, after the subtraction of the Li−Sn contribution to the PDF pattern, broad peaks at around 6−12 Å are present in the PDFs of the lithiated clathrate electrodes at similar positions to the correlations in the PDFs of the Li−Sn compounds, suggesting the presence of analogous but disordered structures in the amorphous phases. We made a similar observation when comparing the PDFs of crystalline Li−Ge binary compounds with those of amorphous phases formed after lithiation of Ba_8Ge_{43} in our previous work.[19] There, we found from PDFs taken during *in situ* heating at 420−450 K that the amorphous lithiated Ba_8Ge_{43} phases crystallized into binary Li−Ge phases. With *in situ* PDF, we demonstrated that the broad correlations from 6 to 10 Å in the amorphous sample were disordered analogues of similar correlations in the crystalline Li−Ge phases. We performed similar *in situ* PDF heating experiments from 300 to 420 K (Figure S9) of the amorphous $Li_{3.2}Ba_{0.17}Ga_{0.33}Sn_{0.67}$, but no significant crystallization events were observed over this temperature range, possibly due to the need for a higher temperature or the complication of Ga being present. Overall, the PDF results show that the local structure of the amorphous Li−Ba−Ga−Sn phase has similarities to those in the crystalline Li−Sn phases. The main difference in the structures is the lack of long-range order and the presence of the Ba−Ga/Sn correlation at 3.60 Å, suggesting that the Ba atoms are intermixed next to Sn/Ga atoms.

3.5. Galvanostatic Cycling. Next, the effect of different lithiation mechanisms on cycling performance for β-Sn and the type VIII clathrate electrodes is compared. Figure 7 shows the voltage profiles, capacity, and Coulombic efficiency (CE) for the two materials for 10 cycles. For β-Sn, the cycling performance is quite poor with a first cycle CE of 55% and low capacity retention, with loss of almost all of the initial capacity by the third cycle. In contrast, the $Ba_8Ga_{15}Sn_{31}$ clathrate shows much better cycling and CE over the 10

https://doi.org/10.1021/acsami.1c07240
ACS Appl. Mater. Interfaces 2021, 13, 42564−42578

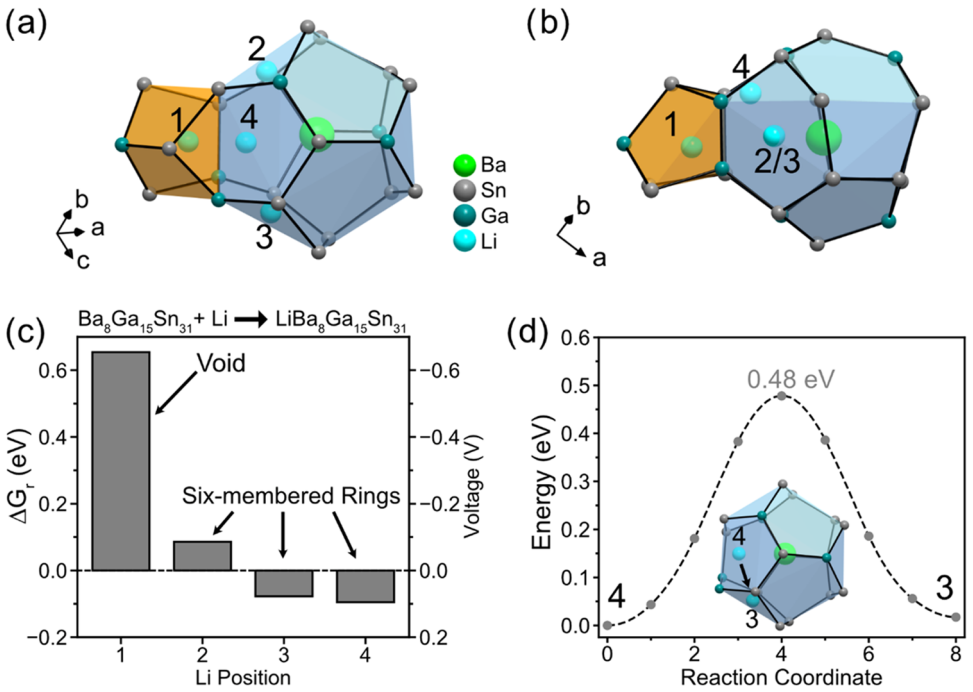

Figure 8. (a, b) Schematics of a void (orange) connected to distorted dodecahedra (blue) in the calculated type VIII $Ba_8Ga_{15}Sn_{31}$ structure with investigated Li positions viewed in two perpendicular directions and labeled 1−4. (c) Gibbs free energy of reaction (ΔG_r) for the reaction $Ba_8Ga_{15}Sn_{31}$ + Li → $LiBa_8Ga_{15}Sn_{31}$ for each different Li position. The corresponding potential (V *vs* Li/Li$^+$) is shown on the right axis. (d) NEB-calculated minimum energy paths for migration of Li (cyan) between positions 4 and 3 in the distorted dodecahedra.

cycles. For the clathrate electrode, the capacity begins at 670 mAh/g and decreases to 75 mAh/g after the 30th cycle, while the CE begins at 75% and then stabilized greater than 95% for the remaining cycles (Figure S10). While detailed investigation of electrolyte reduction processes on the type VIII clathrate surface is out of scope for this work, low CE and insufficiently passivating solid electrolyte interphases (SEI) have been observed before in type I silicon clathrate electrodes[12,46] and may also be the case for the Sn clathrate. We expect, however, that optimization of the electrolyte and electrode construction will allow these materials to have better cycling performance to be competitive with other alloying anode materials.

The voltage profile for the first cycle of β-Sn (Figure 7c) shows the characteristic plateaus described by crystalline phase transformations during lithiation, as described before. However, during the first delithiation, the voltage profile shows a more sloped profile, as well as a lower capacity, resulting in a low CE. Based on the low capacity in subsequent cycles, we presume that the capacity fade originates from electronic disconnection of the β-Sn particles from the current collector due to volume contraction of the Li−Sn compounds during the first delithiation. Previously, an *in operando* NMR study showed that the capacity fade of Sn nanoparticles originated from the disconnection of Li_7Sn_3 during delithiation;[36] we expect this effect to be exacerbated in our case due to the use of larger-sized Sn particles. In contrast, the type VIII clathrate shows a more reversible voltage profile with much better cycling stability, despite the larger initial particle size (Figure S2). The voltage profile of the first delithiation shows a gradually sloped profile from 0.01 to 0.60 V *vs* Li/Li$^+$ with a much higher CE of 75%. In the second cycle, the lithiation curve shows a sloped profile ranging from 0.45 to 0.01 V *vs* Li/Li$^+$ cutoff that mirrors the delithiation profile. In subsequent cycles, the electrode appears to be following the same reaction path due to the similar shape of the voltage profiles, suggesting that after the amorphization of the clathrate in the first cycle, the resulting amorphous phase cycles reversibly. There is still notable capacity fade during electrochemical cycling of the clathrate electrode, which could be due to volume expansion or unstable SEI formation.

Both electrodes were prepared using carbon black and poly(vinylidene difluoride) (PVDF) binder with slightly different active material ratios (80% for $Ba_8Ga_{15}Sn_{31}$ and 90% for β-Sn). Considering the relatively similar electrode construction, the difference in cycling behavior is attributed to differences in the properties of the β-Sn and clathrate-active materials. We attribute the better electrochemical performance of the clathrate phase to the amorphous structural transformation. After the $Ba_8Ga_{15}Sn_{31}$ is converted into an amorphous lithiated phase in the first cycle, subsequent delithiation and lithiation cycles go through solely amorphous solid solutions, which are known to reduce the stress[47−49] experienced by the electrode during lithiation and delithiation, resulting in higher cycling stabilities. Considering the differences in particle sizes and active material ratios, future cycling studies will be needed to fully establish the benefit of the clathrate amorphous phase transformation on the cycling behavior.

3.6. Density Functional Theory (DFT) Calculations.

The aforementioned electrochemical and structural analyses showed that the lithiation process of the type VIII clathrate could be described as a conversion/alloying reaction to an amorphous phase. To assess the possibility of Li insertion into the type VIII $Ba_8Ga_{15}Sn_{31}$ structure prior to electrochemical amorphization, we performed DFT calculations to evaluate the Li site energies and migration barriers between possible Li positions. The type VIII structure is composed of distorted dodecahedra that feature six-membered rings, which are

https://doi.org/10.1021/acsami.1c07240
ACS Appl. Mater. Interfaces 2021, 13, 42564−42578

potentially favorable structural features for Li insertion based on our previous calculations and experiments,[13,16,18,24] as well as voids, which could potentially serve as access points for Li to enter the larger polyhedra. To evaluate the energetic favorability of Li insertion, the Gibbs free energy of reaction (ΔG_r) was calculated for several Li positions where a negative ΔG_r represents a favorable reaction relative to the unlithiated $Ba_8Ga_{15}Sn_{31}$ and Li metal. The pristine clathrate was calculated using the experimental type VIII $Ba_8Ga_{15}Sn_{31}$ unit cell; the Ga substitutions on Sn sites were determined by the occupancy fraction derived from the single-crystal refinement while minimizing Ga−Ga bonds. The resulting structure has a lattice parameter of 11.838 Å (experimental = 11.589 Å) and a formation energy of −0.179 eV/atom. The lattice parameter is in good agreement with our other calculations for tetrel clathrates with the Perdew−Burke−Ernzerhof (PBE) functional, which show a value of around 0.2 Å larger relative to the experimental compound.[18] The hypothetical type VIII Ba_8Sn_{46} structure was also computed and resulted in a much higher formation energy of −0.051 eV/atom, demonstrating how the framework substitution of Ga stabilizes the structure. Then, single Li atoms were placed in the $Ba_8Ga_{15}Sn_{31}$ lattice and relaxed to find the local minimum positions for $LiBa_8Ga_{15}Sn_{31}$. Four Li positions were determined as local minima based on this procedure and are overlaid on the partial structure of the pristine clathrate in Figure 8a,b, which displays a void (shaded orange) connected to the distorted dodecahedra (shaded light blue).

Li position 1 represents Li in the center of the void that forms in between the distorted dodecahedra (as shown more clearly in Figures 1b and 2a). The Gibbs free energy of reaction (ΔG_r) of this position is shown in Figure 8c as Li position "1" with a value of 0.62 eV, suggesting that this position does not result in a favorable reaction. Observation of the Li distances between the unrelaxed (Li−Sn/Ga = 2.22 Å) and relaxed structures (Li−Sn/Ga = 2.54 Å) suggests that the high energy originates from the expansion of the void to maintain acceptable Li−Sn/Ga distances, resulting in significant disturbance of the surrounding Sn/Ge framework. Due to the positive ΔG_r of this position, we conclude that the voids in the type VIII structure are too small to be occupied by Li.

In our previous studies, we identified hexagonal faces as important features for Li to coordinate to or migrate through in clathrate structures.[16,24] In particular, for the guest-free, type I Sn clathrate (Sn_{46}), the center of the hexagonal face was determined as a favorable Li position. Due to the large size of the hexagon composed of Sn atoms,[24] appropriate Li−Sn distances (2.7−2.8 Å) can be maintained. Therefore, we chose to investigate the Li positions in the center of the Sn/Ga six-membered rings in the distorted dodecahedra in the type VIII structure. The energies of the six-membered ring positions are represented by positions 2 and 3; the two positions are distinct because of the different positioning of the adjacent Ga atoms in the six-membered ring (*i.e.*, position 2 has two Ga atoms on opposite sides of the six-membered ring, while position 3 has two Ga bonded together next to the void). The ΔG_r for Li in these positions are +0.06 and −0.087 eV, respectively, suggesting that the local positions of the Ga atoms in the six-membered ring affect the Li site energy. These energies are lower than if Li was placed in the void (position 1) but higher than Li insertion into the Sn_{46} hexagon (−0.30 eV).[24] After relaxation, there is a slight rearrangement of the six-membered ring and the Ba atom in the adjacent cage is perturbed from its original position, suggesting that these disturbances might be the origin of the higher relative energy. Position 4 is also close to a six-membered ring, but this six-membered ring is distorted because part of it forms the void. Similar to position 3, this position has a Gibbs free energy of reaction (ΔG_r) of −0.093 eV, suggesting that the six-membered rings have similar energies for Li insertion. The lattice parameters of the structures after Li insertion are presented in Table S7, which show that relative to the unlithiated structure, the lattice parameter increased by ∼0.04−0.05 Å.

Next, climbing image nudged elastic band (NEB) calculations were used to estimate the Li migration barrier between adjacent Li positions within the distorted dodecahedra. The NEB energy reaction path between positions 4 and 3 is presented in Figure 8d, with the inset showing the beginning and ending Li positions in the cage. The pathway for the migration involves Li moving along the side of the cage, while the Ba atom in the cage moves slightly to maintain its distance from the migrating Li atom. This pathway results in a barrier of 0.48 eV, which is reasonable for room-temperature diffusion,[50] suggesting that Li migration could be feasible within the structure between the six-membered rings of the distorted dodecahedra.

The DFT results suggest that Li insertion is energetically feasible as it predicts Li insertion positions with negative Gibbs free energy (positive voltage *vs* Li/Li^+) with a reasonable migration barrier (0.48 eV) for bulk diffusion. However, whether this process is seen experimentally depends on competing reactions that can occur in a similar voltage range. Since the potential for the alloying reaction of $Ba_8Ga_{15}Sn_{31}$ to form the Li-rich amorphous phase is at 0.25 V *vs* Li/Li^+ (Figure 3), we do not expect Li insertion into the clathrate lattice to occur since alloying occurs at a higher reaction voltage compared to the insertion reactions (*e.g.*, Li insertion into position 3 or 4 at ∼0.10 V *vs* Li/Li^+ per Figure 8c) as the Li content increases. This is further supported by the lack of significant change in the clathrate lattice parameter before and after lithiation, as determined from the PDF refinement (Tables S3 and S6). We attribute the relatively high Li site energies in the $Ba_8Ga_{15}Sn_{31}$ structure to the presence of the Ba guest atoms since our previous calculations showed that the guest-free Sn clathrate (Sn_{46}) has a favorable Li site energy of −0.30 eV. To accommodate the Li atom, the Ba atoms move from their favorable positions in the center of the dodecahedral cages, which incurs an energetic cost to the system and results in a higher-energy Li position compared to that if the Ba was not present. In addition, the Ba and Li atoms are expected to have positive charges, which would repulse and increase the energy of the position. If guest-free type VIII structures could be obtained, they would be particularly interesting for insertion electrodes due to a large amount of six-membered rings in the polyhedra. Unfortunately, there have been few reports of tetrel clathrates forming with the type VIII structure, all of which have a full guest atom occupancy and form with framework substitutions that necessitate guest atoms as electron donors.[22,51−53]

4. DISCUSSION

4.1. Comparison of the Lithiation Mechanisms of Ba_8Ge_{43} and $Ba_8Ga_{15}Sn_{31}$. The structural transformation of the type VIII clathrate $Ba_8Ga_{15}Sn_{31}$ during lithiation is very similar to those observed in our study on type I Ge clathrates.[19] To illustrate this, the voltage profiles, dQ/dE

https://doi.org/10.1021/acsami.1c07240
ACS Appl. Mater. Interfaces 2021, 13, 42564−42578

plots, and PDFs of the fully lithiated structures of $Ba_8Ga_{15}Sn_{31}$ and Ba_8Ge_{43} are presented in Figure 9. Both clathrate voltage

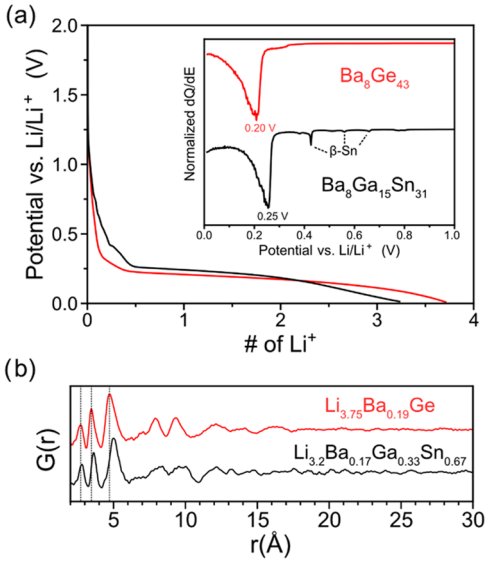

Figure 9. (a) Voltage profile for lithiation of Ba_8Ge_{43} and $Ba_8Ga_{15}Sn_{31}$ and corresponding dQ/dE plots. (b) Comparison of the PDFs from the most lithiated phases of the Ba_8Ge_{43} clathrate and the $Ba_8Ga_{15}Sn_{31}$ clathrate. The compositions are normalized to the amount of nonalkali/alkaline earth metal atoms. The data for Ba_8Ge_{43} are reproduced from ref 19.

profiles show a plateau (seen as a large peak in the dQ/dE plot) followed by a sloped region until the end of lithiation. This shape of voltage profile suggests that upon lithiation, the clathrate phase undergoes a two-phase reaction to form a lithiated amorphous phase, which is further lithiated *via* a solid-solution mechanism. The PDFs of the fully lithiated amorphous phases derived from Ba_8Ge_{43} and $Ba_8Ga_{15}Sn_{31}$ show correlations with similar positions up to 15 Å, with those in $Li_{3.2}Ba_{0.17}Ga_{0.33}Sn_{0.67}$ shifted to slightly higher r values due to the longer bond lengths of Ga and Sn atoms.

The close similarity of the structures and reaction mechanisms for Ba_8Ge_{43} and $Ba_8Ga_{15}Sn_{31}$ during lithiation reveals several important characteristics for the lithiation of Ba-filled clathrates. First, the composition and local structure of the clathrate seem to be more important for the Li alloying reaction rather than the initial crystal structure. While the Ba_8Ge_{43} clathrate is described by the type I and $Ba_8Ga_{15}Sn_{31}$ by the type VIII structure, the spacing of Ba atoms and the local structures are relatively similar. This is illustrated in Figure 10, which shows a schematic of the local structure around Ba atoms that is common to both clathrate structure types with select Ba−Ba distances labeled (Figure 10a) and a unit cell of the Ba sublattice in the type VIII (Figure 10b) and type I (Figure 10c) clathrate structures. The common local feature of the Ba sublattice comprises two face-sharing tetrahedra, which then combine in face-sharing and corner-sharing arrangements in the type VIII structure and in face-sharing arrangements for the type I structure. Both Ba sublattices have similar Ba−Ba distances of around 6 Å, but the distances in Ba_8Ge_{43} show a wider spread as a result of the different Ba sites in the type I structure (corresponding to the centers of the Ge_{20} and Ge_{24} cages). When the clathrate structure is eventually converted to an amorphous phase *via* electrochemical lithiation, the similar local structuring of Ba within the framework structure has a larger effect on the structures of the resulting amorphous phases compared to the small differences in the arrangement of framework/guest atoms in the original clathrate structure.

Another important consideration is that despite differences in composition, both clathrates react through a similar mechanism, as supported by the similarly shaped voltage curves and PDFs after lithiation (Figure 9). The PDF of the framework-substituted, type I clathrate $Ba_8Al_{16}Ge_{30}$ also displayed similar features to that for Ba_8Ge_{43}[19] and $Ba_8Ga_{15}Sn_{31}$ after lithiation. The shared reaction mechanism between the Ba-filled clathrates with different compositions is interesting as elemental Ge,[20] Sn,[32] Al,[54] and Ga[55] all have distinctly different lithiation pathways at room temperature and involve crystallization to Li binary phases. Furthermore, alloys of Sn, such as SnSb[56,57] and GaSn,[58] show electrochemical features during lithiation that can be traced back to the lithiation of the constituent elemental phases, suggesting that significant demixing and crystallization occur during the lithiation process despite the alloyed state of the starting material. We attribute the distinct electrochemical properties of the clathrates to the unique structure where Ba guest atoms and framework atoms form an atomically mixed amorphous phase after lithiation, which kinetically prevents demixing of the constituent elements.

The origin of this amorphous pathway in the lithiation of type VIII clathrate can be attributed to kinetic limitations of the lithiation of the host structure. The Ba atoms are presumed to act as "pillars", which serve to break up long-range order and prevent the bulk crystallization of Li−Sn/Ga phases. This is

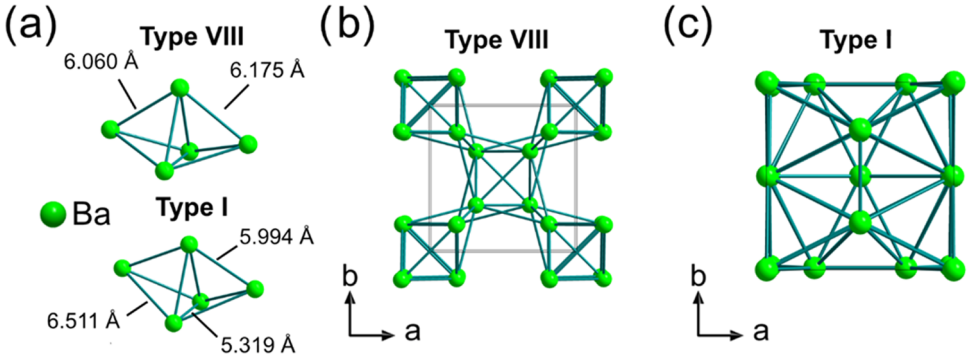

Figure 10. (a) Schematic of the common local structure features in the type VIII $Ba_8Ga_{15}Sn_{31}$ and type I Ba_8Ge_{43} clathrate Ba sublattices. Ba sublattice of the (b) type VIII $Ba_8Ga_{15}Sn_{31}$ clathrate and (c) type I Ba_8Ge_{43} clathrate.

https://doi.org/10.1021/acsami.1c07240
ACS Appl. Mater. Interfaces 2021, 13, 42564−42578

similar to what we observed in the Ba_8Ge_{43} system,[19] but the lack of known binary Ba−Sn clathrate phases (*i.e.*, Ba_8Sn_{43}) precludes a direct comparison to Ba_8Ge_{43}. In contrast, β-Sn undergoes phase transformations at low Li content to form crystalline phases (*e.g.*, Li_2Sn_5, LiSn) that follow the binary phase diagram. Comparison of the crystal structures of β-Sn, Li_2Sn_5, and LiSn (Figure S11) shows a common square Sn unit that is progressively broken up as the Li content increases. It has been suggested that this common feature in the Li−Sn crystalline phases enables kinetically facile phase transformations with good reversibility.[33,35] In the case of the clathrate, the original crystal structure is unrelated to Li−Sn or Li−Ga binary phases, which means that a significant amount of rearrangement and demixing of Ba/Sn/Ga would be required to form crystalline binary phases, a process that is highly unlikely at room temperature. As a result of these kinetic limitations, the phases that form are amorphous with the mobile Li ions driving the structural changes.

The amorphous lithiation pathway of $Ba_8Ga_{15}Sn_{31}$ has significant effects on the voltage profile relative to that in β-Sn. Most notably, the voltage of reaction with lithium is lower for the clathrate (0.25 V *vs* Li/Li^+) than for β-Sn (0.45 V), which is consistent with the formation of a higher-energy amorphous phase. In addition, the presence of Ba and Ga substitutions in the clathrate is expected to further increase the Gibbs free energy of the lithiated phase (*i.e.*, lower the voltage) as seen in our previous study on the $Ba_8Al_yGe_{46-y}$ ($0 < y < 16$) clathrates, which demonstrated that increasing Al substitution decreased the reaction potential compared to Ba_8Ge_{43}.[18] We speculate that Ga substitution could have a similar effect on the reaction potential. We also note that the clathrate reacts with a lower amount of Li compared to β-Sn (3.2 Li for the clathrate, 3.4 Li for β-Sn), which was also a notable effect when increasing the degree of Al substitution in $Ba_8Al_yGe_{46-y}$.

After the initial conversion of the clathrate to an amorphous phase in the first cycle, the delithiation profile is sloped, showing no distinct plateaus corresponding to phase transformations. This sloped behavior suggests that delithiation of the $Li_xBa_{0.17}Ga_{0.33}Sn_{0.67}$ phase goes through a solid-solution mechanism where the Li content varies continuously during the reaction. After one lithiation and delithiation cycle, the originally crystalline clathrate is suspected to now be amorphous, similar to what occurs for diamond cubic Si.[47,48] From the PDF analysis of Ba_8Ge_{43} after full lithiation and delithiation, the local structure was found to be similar to that of the original pristine crystalline clathrate but did not exhibit long-range order. On the basis of the similar reaction mechanisms we have observed in the Ba-containing clathrates, we expect delithiated $Li_xBa_{0.17}Ga_{0.33}Sn_{0.67}$ to have a similarly structured amorphous phase. During cycling, the shape of the voltage profile does not change significantly, suggesting that the amorphous phase formed in the first cycle is able to be reversibly cycled. However, future PDF characterization after cycling or *in situ* measurements will be needed to confirm this.

4.2. Design Strategies for Li-Ion Battery Applications. Given that Ba_8Ge_{43}, $Ba_8Al_{16}Ge_{30}$, and $Ba_8Ga_{15}Sn_{31}$ all undergo amorphous phase transformations upon reaction with Li, we presume that this amorphous reaction mechanism might be a general feature of Li alloying with guest-filled clathrates. An exception to this trend is the type I clathrate $Ba_8Al_{16}Si_{30}$, which we found to display electrochemical reactions dominated by surface reactions rather than bulk alloying reactions.[12,15] Notably, the presence of guest atoms is important as clathrates with type II structures that can be synthesized without guest atoms (*i.e.* vacant cages) can go through topotactic insertion reactions without transforming to amorphous phases at low degrees of lithiation. This has been observed in Si_{136}[9,16] and also likely occurs in Ge_{136},[17] but amorphous phase transformations are observed if the type II clathrates are prepared with guest atoms[11] or overlithiated.[16] On the basis of the DFT calculations presented herein (Figure 8) and our previous calculations, we conclude that clathrates with occupied cages will favor amorphous phase transformations over insertion reactions since the energies for the Li sites (for insertion processes) and migration barriers increase if the cages are already occupied.[13,18,24] By assuming a common amorphous reaction mechanism among clathrates containing guest atoms, we can propose a general strategy for designing clathrates to serve as alloying anodes, which could be helpful in directing future research. First, it is important to emphasize that the initial crystalline clathrate structure will be converted into an amorphous phase in the first lithiation process and later cycles will involve lithiation/delithiation of amorphous phases. This is similar to the electrochemical reaction of Li with diamond cubic Si, where the diamond structure is not recovered after Li is removed.[47,48,59] Next, the guest atoms (*i.e.*, Ba) in the clathrate structure serve as electrochemically inactive but structurally important components, with the role of kinetically frustrating the formation of crystalline phases. Suppressing the formation of crystalline phases mitigates large changes in volume, which can lead to better cycling retention. Then, substitution of elements on tetrel framework sites (*i.e.*, with Ga or Al) allows for tuning of the reaction voltage and lithiation capacity of the amorphous phase.

In terms of the guest atom selection, the optimal choice is the lightest atom possible to maintain a high gravimetric specific capacity while still having the benefit of serving as "pillar" to suppress crystalline phase transformations. In this regard, the lightest reported guest atom (other than Li) for clathrates is Na.[1] However, our previous studies investigating the properties of Na-filled Si clathrates in batteries suggest that the Na guest atom does not suppress crystalline phase transformations, as the formation of crystalline $Li_{15}Si_4$ was observed after full lithiation of both type I (Na_8Si_{46}) and type II ($Na_{24}Si_{136}$) clathrates.[11,14] The lithiation of Na-filled Ge clathrates (*e.g.*, $Na_{24-x}Ge_{136}$,[5,60] $Na_8Zn_4Ge_{42}$,[61] $Na_8Ga_8Ge_{38}$[62]) has yet to be reported but would be promising if phase transformations were disrupted. However, we think this is unlikely as Ge generally shows a higher propensity than Si to undergo crystalline phase transformations during lithiation, at least when adopting the diamond cubic structure. The next lightest guest atom for clathrates is K, with many K-filled Si, Ge, and Sn clathrates reported.[63−66] We believe that K-filled clathrates are particularly promising due to the significantly larger atomic size of K compared to that of Na, which might affect the room-temperature lithiation pathway significantly while still having a relatively low atomic weight. We have preliminary data of the K-containing Ge clathrate, $K_8Li_xGe_{46-x}$,[67] showing that the voltage profile displays a single major plateau during lithiation and then a sloped delithiation curve (Figure S12a,b), similar to Ba_8Ge_{43} and $Ba_8Ga_{15}Sn_{31}$, suggesting that it might also go through an amorphous phase transformation. PXRD after full lithiation showed that the pristine clathrate reflections decreased in intensity without any other phases being detected, further supporting an amorphous phase transformation (Figure S12c).

https://doi.org/10.1021/acsami.1c07240
ACS Appl. Mater. Interfaces 2021, 13, 42564−42578

Due to the large particle sizes of the $K_8Li_xGe_{46-x}$ (Figure S12d,e), we suspect that there could be kinetic limitations during the lithiation, which resulted in incomplete conversion of the clathrate. Further structural characterization with PDF analysis of the lithiation intermediates of $K_8Li_xGe_{46-x}$ will be needed to confirm the suspected amorphous phase transformation. Tetrel clathrates have also been reported with Rb, Cs, Ca, Sr, and rare-earth guest atoms;[1,68−72] however, these guest atoms are heavier than K and Na and would be less attractive in terms of gravimetric capacity. More work examining the effect of the size and valency of the guest atom on the subsequent lithiation pathways would be warranted for assessing the viability of heavier guest atoms.

Substitution of framework atoms with other elements is also an interesting design avenue as it allows for tuning of the reaction capacity/voltage while also being able to compensate for the extra mass originating from the guest atoms. In the case of $Ba_8Ga_{15}Sn_{31}$, the molar mass (5829.3 g/mol) is lower than that of pure Sn (6409.8 g/mol) on a per-atom basis, meaning that the additional mass from Ba atoms is negated by the incorporation of the Ga. This means that despite the lower amount of Li reacting with $Ba_8Ga_{15}Sn_{31}$ (3.2 Li per Sn/Ga *vs* 3.4 Li per Sn for β-Sn as seen in our results), both $Ba_8Ga_{15}Sn_{31}$ and β-Sn have similar initial capacities (~700 mAh/g). In addition to the modification of the capacity in terms of weight or amount of reacted Li, our findings suggest that adding substitutions decreases the reaction voltage (also seen when substituting Al for Ge in $Ba_8Al_yGe_{46-y}$),[18,19] which would result in a higher overall cell voltage when the clathrate is coupled with a cathode in a full cell, resulting in a higher energy density. The effect of substitutions on the capacity, reaction voltage, and amount of Li that can react with the electrode means that there should be an optimal point at which the energy density is maximized. Considering the K-filled Ge and Sn clathrates, Al-substituted clathrates such as $K_8Al_8Ge_{38}$ and $K_8Al_8Sn_{38}$[73] are particularly promising due to the low weight of Al, which could nullify the weight increase from K while also potentially decreasing the reaction voltage with minimal decreases to the amount of Li that reacts. If these clathrates go through amorphous lithiation pathways like the Ba clathrates, then they could be promising alternatives to elemental Ge and Sn anodes for Li-ion batteries.

5. CONCLUSIONS

In this work, the lithiation pathway of the type VIII $Ba_8Ga_{15}Sn_{31}$ clathrate is investigated with electrochemical analysis and total scattering X-ray powder diffraction measurements. $Ba_8Ga_{15}Sn_{31}$ and β-Sn (as a comparison) are lithiated to similar amounts and then subjected to X-ray characterization. The lithiation voltage profile for the type VIII clathrate shows a single plateau at 0.25 V followed by a sloping profile, while the voltage profile of β-Sn has three plateaus corresponding to known phase transformations to Li−Sn crystalline phases. Structure function patterns at different points in lithiation confirm that β-Sn goes through crystalline phase transformations, while the type VIII clathrate undergoes an amorphous phase transition. PDF analysis confirms the phase transformation of the type VIII $Ba_8Ga_{15}Sn_{31}$ clathrate to a highly lithiated amorphous phase that lacks long-range order. The PDF analysis also suggests that the amorphous $Li_xBa_{0.17}Ga_{0.33}Sn_{0.67}$ phases share similar local structures to those in crystalline Li−Sn phases. Galvanostatic cycling experiments showed that the type VIII clathrate resulted in better cycling and Coulombic efficiency than β-Sn, which is attributed to reduced stresses and deleterious effects of volume expansion/contraction during cycling on account of the solid-solution lithiation/delithiation mechanism in the clathrate electrode. DFT calculations to assess the possibility of topotactic Li insertion into the $Ba_8Ga_{15}Sn_{31}$ clathrate suggest that the Li insertion site energy is too high to be competitive with the amorphous alloying reaction due to the presence of the Ba guest atoms in the cages.

Overall, we find that the lithiation of the type VIII $Ba_8Ga_{15}Sn_{31}$ is very similar to that observed in the type I Ba_8Ge_{43} clathrate investigated in our previous work. The similar reaction mechanism and structure of the amorphous phases are attributed to the unique clathrate structure in which Ba atoms are distributed through the cage framework and act as "pillars" to prevent long-range ordering. The resulting amorphous phase has distinct electrochemical reactions with Li relative to those in the elemental phases and potentially beneficial electrochemical properties such as a lower reaction voltage and better cycling stability due to the solid-solution mechanism. Tetrel clathrates represent a wide design space for tuning the material properties because of the numerous types of guest atoms, structures, and compositions. Based on the results presented here, we expect that many other clathrate compositions could undergo amorphous alloying reactions with novel and tunable electrochemical properties for Li-ion battery applications.

■ ASSOCIATED CONTENT

Supporting Information

The Supporting Information is available free of charge at https://pubs.acs.org/doi/10.1021/acsami.1c07240.

Detailed experimental procedures for the synthesis of type VIII clathrate, electrochemical measurements, sample preparation for synchrotron measurements, pair distribution function analysis, powder X-ray diffraction and scanning electron microscopy, and density functional theory calculations; supporting tables include crystallographic data for $Ba_8Ga_{14.9}Sn_{31.1}$ from single-crystal XRD; PDFgui refinement parameters for pristine $Ba_8Ga_{15}Sn_{31}$ and pristine β-Sn, and Li_xSn and $Li_xBa_{0.17}Ga_{0.33}Sn_{0.67}$ samples fit to different phase combinations; the measured voltages and capacity for each sample after electrochemical lithiation; and lattice constants from the DFT-calculated structures (Li-$Ba_8Ga_{15}Sn_{31}$); supporting figures include SEM images and EDS of two $Ba_8Ga_{15}Sn_{31}$ single-crystal particles; PXRD of the hand-ground type VIII crystals; SEM images of $Ba_8Ga_{15}Sn_{31}$ and β-Sn electrodes prior to electrochemical lithiation; calculated total and partial PDF patterns for LiSn, Li_7Sn_3, Li_7Sn_2, and type VIII clathrate $Ba_8Ga_{15}Sn_{31}$; crystal model schematics of β-Sn, LiSn, Li_2Sn_5, and Li_7Sn_3; PDF refinements for pristine β-Sn, lithiated β-Sn (Li_xSn) samples, and lithiated $Ba_8Ga_{15}Sn_{31}$ ($Li_xBa_{0.17}Ga_{0.33}Sn_{0.67}$) samples; variable temperature PDF during *in situ* heating from 310 to 420 K for $Li_{3.2}Ba_{0.17}Ga_{0.33}Sn_{0.67}$; capacity and Coulombic efficiency *vs* cycle number for β-Sn and the type VIII $Ba_8Ga_{15}Sn_{31}$ clathrate for 30 cycles; and voltage profile, dQ/dE plot, PXRD, and SEM of type I $K_8Li_xGe_{44-x}$ clathrate electrode before and after full lithiation (PDF)

https://doi.org/10.1021/acsami.1c07240
ACS Appl. Mater. Interfaces 2021, 13, 42564−42578

CIF for the single-crystal XRD refinement of the as-synthesized $Ba_8Ga_{15}Sn_{31}$ (CIF)
CIF for the DFT-calculated structure of $Ba_8Ga_{15}Sn_{31}$ (CIF)

AUTHOR INFORMATION

Corresponding Author

Candace K. Chan − *Materials Science and Engineering, School for Engineering of Matter, Transport and Energy, Arizona State University, Tempe, Arizona 85827, United States; Department of Heterogenous Catalysis, Max-Planck-Institut für Kohlenforschung, 45470 Mülheim an der Ruhr, Germany;* orcid.org/0000-0003-4329-4865; Phone: (480) 727-8614; Email: candace.chan@asu.edu

Authors

Andrew Dopilka − *Materials Science and Engineering, School for Engineering of Matter, Transport and Energy, Arizona State University, Tempe, Arizona 85827, United States*

Amanda Childs − *Department of Chemistry and Biochemistry, University of Delaware, Newark, Delaware 19716, United States*

Alexander Ovchinnikov − *Department of Chemistry and Biochemistry, University of Delaware, Newark, Delaware 19716, United States; Department of Materials and Environmental Chemistry, Stockholm University, 10691 Stockholm, Sweden;* orcid.org/0000-0002-0537-4234

Ran Zhao − *School of Molecular Sciences, Arizona State University, Tempe, Arizona 85287, United States*

Svilen Bobev − *Department of Chemistry and Biochemistry, University of Delaware, Newark, Delaware 19716, United States;* orcid.org/0000-0002-0780-4787

Xihong Peng − *College of Integrative Sciences and Arts, Arizona State University Polytechnic Campus, Mesa, Arizona 85212, United States*

Complete contact information is available at: https://pubs.acs.org/10.1021/acsami.1c07240

Author Contributions

The manuscript was written through contributions of all authors. A.O. and R.Z. performed the clathrate synthesis. A.D. and R.Z. prepared the electrodes and performed the electrochemical measurements and laboratory PXRD. A.D., A.C., and C.K.C. performed the sample preparation and conducted the synchrotron measurements. A.C. and S.B. performed the single-crystal XRD and refinement. A.D. and X.P. performed the DFT calculations. C.K.C. assisted A.D. with the electrochemical and PDF analyses. C.K.C., S.B., and X.P. conceived the project. All authors have given approval to the final version of the manuscript.

Funding

Open access funded by Max Planck Society.

Notes

The authors declare no competing financial interest.

ACKNOWLEDGMENTS

This work was supported by funding from NSF from the awards DMR-1206795, DMR-1710017, DMR-1709813, DMR-2004514, and DMR-2004579. A.D. acknowledges support from the ASU Fulton Schools of Engineering Dean's Fellowships. C.K.C. acknowledges support from the Max Planck Society and the Alexander von Humboldt Foundation for a Humboldt Research Fellowship. The authors acknowledge the use of facilities within the Erying Materials Center at Arizona State University supported, in part, by NNCI-ECCS-1542160. The authors acknowledge the use of the Research Computing at Arizona State University for providing high-performance computing resources that have contributed to the research results reported within this article. The authors thank J. Guo for assistance with the SEM measurements. The authors also thank the Diamond Light Source (Didcot, U.K.) for access to beamline I15-1 (proposal no. CY22209) and T. Forrest and D. Keeble for assistance with PDF measurements.

REFERENCES

(1) Dolyniuk, J.; Owens-Baird, B.; Wang, J.; Zaikina, J. V.; Kovnir, K. Clathrate Thermoelectrics. *Mater. Sci. Eng., R* **2016**, *108*, 1−46.
(2) Christensen, M.; Johnsen, S.; Iversen, B. B. Thermoelectric Clathrates of Type I. *Dalton Trans.* **2010**, *39*, 978−992.
(3) Hübner, J. M.; Prots, Y.; Schnelle, W.; Bobnar, M.; König, M.; Baitinger, M.; Simon, P.; Carrillo-Cabrera, W.; Ormeci, A.; Svanidze, E.; Grin, Y.; Schwarz, U. In-Cage Interactions in the Clathrate Superconductor Sr_8Si_{46}. *Chem. − Eur. J.* **2020**, *26*, 830−838.
(4) Kawaji, H.; Horie, H.; Yamanaka, S.; Ishikawa, M. Superconductivity in the Silicon Clathrate Compound $(Na, Ba)_xSi_{46}$. *Phys. Rev. Lett.* **1995**, *74*, 1427−1429.
(5) Baranowski, L. L.; Krishna, L.; Martinez, A. D.; Raharjo, T.; Stevanović, V.; Tamboli, A. C.; Toberer, E. S. Synthesis and Optical Band Gaps of Alloyed Si−Ge Type II Clathrates. *J. Mater. Chem. C* **2014**, *2*, 3231−3237.
(6) Martinez, A. D.; Krishna, L.; Baranowski, L. L.; Lusk, M. T.; Toberer, E. S.; Tamboli, A. C. Synthesis of Group IV Clathrates for Photovoltaics. *IEEE J. Photovoltaics* **2013**, *3*, 1305−1310.
(7) Kume, T.; Ohashi, F.; Sakai, K.; Fukuyama, A.; Imai, M.; Udono, H.; Ban, T.; Habuchi, H.; Suzuki, H.; Ikari, T.; Sasaki, S.; Nonomura, S. Thin Film of Guest-Free Type-II Silicon Clathrate on Si(111) Wafer. *Thin Solid Films* **2016**, *609*, 30−34.
(8) Baitinger, M.; Böhme, B.; Wagner, F. R.; Schwarz, U. Zintl Defects in Intermetallic Clathrates. *Z. Anorg. Allg. Chem.* **2020**, *646*, 1034−1041.
(9) Langer, T.; Dupke, S.; Trill, H.; Passerini, S.; Eckert, H.; Pöttgen, R.; Winter, M. Electrochemical Lithiation of Silicon Clathrate-II. *J. Electrochem. Soc.* **2012**, *159*, A1318−A1322.
(10) Yang, J.; Tse, J. S. Silicon Clathrates as Anode Materials for Lithium Ion Batteries? *J. Mater. Chem. A* **2013**, *1*, 7782−7789.
(11) Wagner, N. A.; Raghavan, R.; Zhao, R.; Wei, Q.; Peng, X.; Chan, C. K. Electrochemical Cycling of Sodium-Filled Silicon Clathrate. *ChemElectroChem* **2014**, *1*, 347−353.
(12) Li, Y.; Raghavan, R.; Wagner, N. A.; Davidowski, S. K.; Baggetto, L.; Zhao, R.; Cheng, Q.; Yarger, J. L.; Veith, G. M.; Ellis-Terrell, C.; Miller, M. A.; Chan, K. S.; Chan, C. K. Type I Clathrates as Novel Silicon Anodes: An Electrochemical and Structural Investigation. *Adv. Sci.* **2015**, *2*, No. 1500057.
(13) Peng, X.; Wei, Q.; Li, Y.; Chan, C. K. First-Principles Study of Lithiation of Type I Ba-Doped Silicon Clathrates. *J. Phys. Chem. C* **2015**, *119*, 28247−28257.
(14) Dopilka, A.; Childs, A.; Bobev, S.; Chan, C. K. Solid-State Electrochemical Synthesis of Silicon Clathrates Using a Sodium-Sulfur Battery Inspired Approach. *J. Electrochem. Soc.* **2021**, *168*, No. 020516.
(15) Zhao, R.; Bobev, S.; Krishna, L.; Yang, T.; Weller, J. M.; Jing, H.; Chan, C. K. Anodes for Lithium-Ion Batteries Based on Type I Silicon Clathrate $Ba_8Al_{16}Si_{30}$ - Role of Processing on Surface Properties and Electrochemical Behavior. *ACS Appl. Mater. Interfaces* **2017**, *9*, 41246−41257.
(16) Dopilka, A.; Weller, J. M.; Ovchinnikov, A.; Childs, A.; Bobev, S.; Peng, X.; Chan, C. K. Structural Origin of Reversible Li Insertion in Guest-Free, Type-II Silicon Clathrates. *Adv. Energy Sustainable Res.* **2021**, *2*, No. 2000114.
(17) Böhme, B.; Minella, C. B.; Thoss, F.; Lindemann, I.; Rosenburg, M.; Pistidda, C.; Møller, K. T.; Jensen, T. R.; Giebeler,

L.; Baitinger, M.; Gutfleisch, O.; Ehrenberg, H.; Eckert, J.; Grin, Y.; Schultz, L. B1-Mobilstor: Materials for Sustainable Energy Storage Techniques - Lithium Containing Compounds for Hydrogen and Electrochemical Energy Storage. *Adv. Eng. Mater.* **2014**, *16*, 1189−1195.
(18) Dopilka, A.; Zhao, R.; Weller, J. M.; Bobev, S.; Peng, X.; Chan, C. K. Experimental and Computational Study of the Lithiation of $Ba_8Al_yGe_{46-y}$ Based Type I Germanium Clathrates. *ACS Appl. Mater. Interfaces* **2018**, *10*, 37981−37993.
(19) Dopilka, A.; Childs, A.; Bobev, S.; Chan, C. K. Understanding the Amorphous Lithiation Pathway of the Type I Ba_8Ge_{43} Clathrate with Synchrotron X-Ray Characterization. *Chem. Mater.* **2020**, *32*, 9444−9457.
(20) Jung, H.; Allan, P. K.; Hu, Y. Y.; Borkiewicz, O. J.; Wang, X. L.; Han, W. Q.; Du, L. S.; Pickard, C. J.; Chupas, P. J.; Chapman, K. W.; Morris, A. J.; Grey, C. P. Elucidation of the Local and Long-Range Structural Changes That Occur in Germanium Anodes in Lithium-Ion Batteries. *Chem. Mater.* **2015**, *27*, 1031−1041.
(21) Shevelkov, A. V.; Kovnir, K. Zintl Clathrates. In *Zintl Phases: Principles and Recent Developments*; Fässler, T. F., Ed.; Springer: Berlin, Heidelberg, 2011; pp 97−142.
(22) Eisenmann, B.; Schäfer, H.; Zagler, R. Die Verbindungen $A_8^{II}B_{16}^{III}B_{30}^{IV}$ (AII = Sr, Ba; BIII =Al, Ga; BIV= Si, Ge, Sn) Und Ihre Käfigstrukturen. *J. Less-Common Met.* **1986**, *118*, 43−55.
(23) Schäfer, M. C.; Yamasaki, Y.; Fritsch, V.; Bobev, S. Ternary Compounds in the Sn-Rich Section of the Ba−Ga−Sn System: $Ba_8Ga_{16-x}Sn_{30+x}$ ($1.1 \leq x \leq 2.8$) Clathrates of Type-I and Type-VIII, and $BaGa_{2-x}Sn_{4+x}$ ($x \approx 0.2$) with a Clathrate-like Structure. *Crystals* **2011**, *1*, 145−162.
(24) Dopilka, A.; Peng, X.; Chan, C. K. Ab Initio Investigation of Li and Na Migration in Guest-Free, Type I Clathrates. *J. Phys. Chem. C* **2019**, *123*, 22812−22822.
(25) Farrow, C. L.; Billinge, S. J. L. Relationship between the Atomic Pair Distribution Function and Small-Angle Scattering: Implications for Modeling of Nanoparticles. *Acta Crystallogr., Sect. A: Found. Crystallogr.* **2009**, *65*, 232−239.
(26) Juhás, P.; Davis, T.; Farrow, C. L.; Billinge, S. J. L. PDFgetX3: A Rapid and Highly Automatable Program for Processing Powder Diffraction Data into Total Scattering Pair Distribution Functions. *J. Appl. Crystallogr.* **2013**, *46*, 560−566.
(27) Yang, X.; Juhas, P.; Farrow, C. L.; Billinge, S. J. L. xPDFsuite: An End-to-End Software Solution for High Throughput Pair Distribution Function Transformation, Visualization and Analysis. 2014, arXiv:1402.3163. arXiv.org e-Print archive. https://arxiv.org/abs/1402.3163.
(28) Henkelman, G.; Uberuaga, B. P.; Jónsson, H. Climbing Image Nudged Elastic Band Method for Finding Saddle Points and Minimum Energy Paths. *J. Chem. Phys.* **2000**, *113*, 9901−9904.
(29) Predel, B. Zustandsdiagramm und Eigenschaften von Gallium-Zinn-Legierungen. *J. Less-Common Met.* **1964**, *7*, 347−355.
(30) Hansen, D. A.; Chang, L. J. Crystal Structure of Li_2Sn_5. *Acta Crystallogr., Sect. B: Struct. Crystallogr. Cryst. Chem.* **1969**, *25*, 2392−2395.
(31) Müller, W.; Schäfer, H. Die Kristallstruktur Der Phase LiSn: The Crystal Structure of LiSn. *Z. Naturforsch., B* **1973**, *28*, 246−248.
(32) Courtney, I. A.; Tse, J. S.; et al. Ab Initio Calculation of the Lithium-Tin Voltage Profile. *Phys. Rev. B: Condens. Matter Mater. Phys.* **1998**, *58*, 15583−15588.
(33) Courtney, I. A.; Dahn, J. R. Electrochemical and In Situ X-Ray Diffraction Studies of the Reaction of Lithium with Tin Oxide Composites. *J. Electrochem. Soc.* **1997**, *144*, 2045−2052.
(34) Ichitsubo, T.; Yukitani, S.; Hirai, K.; Yagi, S.; Uda, T.; Matsubara, E. Mechanical-Energy Influences to Electrochemical Phenomena in Lithium-ion Batteries. *J. Mater. Chem.* **2011**, *21*, 2701−2708.
(35) Rhodes, K. J.; Meisner, R.; Kirkham, M.; Dudney, N.; Daniel, C. In Situ XRD of Thin Film Tin Electrodes for Lithium Ion Batteries. *J. Electrochem. Soc.* **2012**, *159*, A294−A299.
(36) Lorie Lopez, J. L.; Grandinetti, P. J.; Co, A. C. Phase Transformations and Capacity Fade Mechanism in Li_xSn Nanoparticle Electrodes Revealed by Operando ^7Li NMR. *J. Mater. Chem. A* **2019**, *7*, 10781−10794.
(37) Chouvin, J.; Olivier-Fourcade, J.; Jumas, J.; Simon, B.; Godiveau, O. ^{119}Sn Mössbauer Study of Li_xSn Alloys Prepared Electrochemically. *Chem. Phys. Lett.* **1999**, *308*, 413−420.
(38) Lupu, C.; Mao, J. G.; Rabalais, J. W.; Guloy, A. M.; Richardson, J. W. X-Ray and Neutron Diffraction Studies on "$Li_{4.4}Sn$". *Inorg. Chem.* **2003**, *42*, 3765−3771.
(39) Dahn, J. R.; Courtney, I. A.; Mao, O. Short-Range Sn Ordering and Crystal Structure of $Li_{4.4}Sn$ Prepared by Ambient Temperature Electrochemical Methods. *Solid State Ionics* **1998**, *111*, 289−294.
(40) Oehl, N.; Schmuelling, G.; Knipper, M.; Kloepsch, R.; Placke, T.; Kolny-Olesiak, J.; Plaggenborg, T.; Winter, M.; Parisi, J. In Situ X-Ray Diffraction Study on the Formation of α-Sn in Nanocrystalline Sn-Based Electrodes for Lithium-Ion Batteries. *CrystEngComm* **2015**, *17*, 8500−8504.
(41) Müller, W. Preparation Und Crystal Structure of Li_7Sn_3. *Z. Naturforsch., B* **1974**, *29*, 304−311.
(42) Key, B.; Morcrette, M.; Tarascon, J.-M.; Grey, C. P. Pair Distribution Function Analysis and Solid State NMR Studies of Silicon Electrodes for Lithium Ion Batteries: Understanding the (De)Lithiation Mechanisms. *J. Am. Chem. Soc.* **2011**, *133*, 503−512.
(43) Jung, H. Solid State NMR and Pair Distribution Function Analysis Studies of Ge and Sn Anodes for Li-Ion Batteries. Ph.D. Thesis, Stony Brook University: Stony Brook, 2015.
(44) Allan, P. K.; Griffin, J. M.; Darwiche, A.; Borkiewicz, O. J.; Wiaderek, K. M.; Chapman, K. W.; Morris, A. J.; Chupas, P. J.; Monconduit, L.; Grey, C. P. Tracking Sodium-Antimonide Phase Transformations in Sodium-Ion Anodes: Insights from Operando Pair Distribution Function Analysis and Solid-State NMR Spectroscopy. *J. Am. Chem. Soc.* **2016**, *138*, 2352−2365.
(45) Stratford, J. M.; Mayo, M.; Allan, P. K.; Pecher, O.; Borkiewicz, O. J.; Wiaderek, K. M.; Chapman, K. W.; Pickard, C. J.; Morris, A. J.; Grey, C. P. Investigating Sodium Storage Mechanisms in Tin Anodes: A Combined Pair Distribution Function Analysis, Density Functional Theory, and Solid-State NMR Approach. *J. Am. Chem. Soc.* **2017**, *139*, 7273−7286.
(46) Tarnev, T.; Wilde, P.; Dopilka, A.; Schuhmann, W.; Chan, C. K.; Ventosa, E. Surface Properties of Battery Materials Elucidated Using Scanning Electrochemical Microscopy: The Case of Type I Silicon Clathrate. *ChemElectroChem* **2020**, *7*, 665−671.
(47) Obrovac, M. N.; Christensen, L. Structural Changes in Silicon Anodes during Lithium Insertion/Extraction. *Electrochem. Solid-State Lett.* **2004**, *7*, A93−A96.
(48) McDowell, M. T.; Lee, S. W.; Nix, W. D.; Cui, Y. 25th Anniversary Article: Understanding the Lithiation of Silicon and Other Alloying Anodes for Lithium-Ion Batteries. *Adv. Mater.* **2013**, *25*, 4966−4985.
(49) Hatchard, T. D.; Topple, J. M.; Fleischauer, M. D.; Dahn, J. R. Electrochemical Performance of SiAlSn Films Prepared by Combinatorial Sputtering. *Electrochem. Solid-State Lett.* **2003**, *6*, A129.
(50) Rong, Z.; Malik, R.; Canepa, P.; Sai Gautam, G.; Liu, M.; Jain, A.; Persson, K.; Ceder, G. Materials Design Rules for Multivalent Ion Mobility in Intercalation Structures. *Chem. Mater.* **2015**, *27*, 6016−6021.
(51) Kishimoto, K.; Ikeda, N.; Akai, K.; Koyanagi, T. Synthesis and Thermoelectric Properties of Silicon Clathrates $Sr_8Al_xGa_{16-x}Si_{30}$ with the Type-I and Type-VIII Structures. *Appl. Phys. Express* **2008**, *1*, No. 031201.
(52) Paschen, S.; Carrillo-Cabrera, W.; Bentien, A.; Tran, V. H.; Baenitz, M.; Grin, Y.; Steglich, F. Structural, Transport, Magnetic, and Thermal Properties of $Eu_8Ga_{16}Ge_{30}$. *Phys. Rev. B: Condens. Matter Mater. Phys.* **2001**, *64*, 1−11.
(53) Sasaki, Y.; Kishimoto, K.; Koyanagi, T.; Asada, H.; Akai, K. Synthesis and Thermoelectric Properties of Type-VIII Germanium Clathrates $Sr_8Al_xGa_yGe_{46-x-y}$. *J. Appl. Phys.* **2009**, *105*, No. 073702.

(54) Hamon, Y.; Brousse, T.; Jousse, F.; Topart, P.; Buvat, P.; Schleich, D. M. Aluminum Negative Electrode in Lithium Ion Batteries. *J. Power Sources* **2001**, *97*−*98*, 185−187.
(55) Lee, K. T.; Jung, Y. S.; Kim, T.; Kim, C. H.; Kim, J. H.; Kwon, J. Y.; Oh, S. M. Liquid Gallium Electrode Confined in Porous Carbon Matrix as Anode for Lithium Secondary Batteries. *Electrochem. Solid-State Lett.* **2008**, *11*, A21−A24.
(56) Besenhard, J. O.; Yang, J.; Winter, M. Will Advanced Lithium-Alloy Anodes Have a Chance in Lithium-Ion Batteries? *J. Power Sources* **1997**, *68*, 87−90.
(57) Yang, J.; Takeda, Y.; Imanishi, N.; Yamamoto, O. Ultrafine Sn and $SnSb_{0.14}$ Powders for Lithium Storage Matrices in Lithium-Ion Batteries. *J. Electrochem. Soc.* **1999**, *146*, 4009−4013.
(58) Wu, Y.; Huang, L.; Huang, X.; Guo, X.; Liu, D.; Zheng, D.; Zhang, X.; Ren, R.; Qu, D.; Chen, J. A Room-Temperature Liquid Metal-Based Self-Healing Anode for Lithium-Ion Batteries with an Ultra-Long Cycle Life. *Energy Environ. Sci.* **2017**, *10*, 1854−1861.
(59) Obrovac, M. N.; Krause, L. J. Reversible Cycling of Crystalline Silicon Powder. *J. Electrochem. Soc.* **2007**, *154*, A103−A108.
(60) Böhme, B. An Electrochemical Approach toward the Metastable Type II Clathrate Germanium Allotrope. *Inorg. Chem.* **2020**, *59*, 11920−11924.
(61) Stegmaier, S.; Hlukhyy, V.; Fässler, T. F. The Intermetallic Type-I Clathrate $Na_8Zn_4Ge_{42}$. *Z. Anorg. Allg. Chem.* **2020**, *646*, 1073−1078.
(62) Takeshita, R.; Kishimoto, K.; Asada, H.; Akai, K. Thermoelectric Properties of Type-I Clathrate $Na_8Ga_8Ge_{38}$. *J. Solid State Chem.* **2021**, *294*, No. 121911.
(63) Beekman, M.; Nolas, G. S. Transport Properties of the Binary Type I Clathrate $K_8Ge_{44}\square_2$. *Int. J. Appl. Ceram. Technol.* **2007**, *4*, 332−338.
(64) Ramachandran, G. K.; McMillan, P. F.; Dong, J.; Sankey, O. F. $K_{7.62(1)}Si_{46}$ and $Rb_{6.15(2)}Si_{46}$: Two Structure I Clathrates with Fully Occupied Framework Sites. *J. Solid State Chem.* **2000**, *154*, 626−634.
(65) Møllnitz, L.; Blake, N. P.; Meitu, H. Effects of Morphology on the Electronic and Transport Properties of Sn-Based Clathrates. *J. Chem. Phys.* **2002**, *117*, 1302−1312.
(66) Krishna, L.; Chai, P.; Koh, C. A.; Toberer, E. S.; Nolas, G. S. Synthesis and Structural Properties of Type I Potassium SiGe Alloy Clathrates. *Mater. Lett.* **2015**, *149*, 123−126.
(67) Liang, Y.; Böhme, B.; Ormeci, A.; Borrmann, H.; Pecher, O.; Haarmann, F.; Schnelle, W.; Baitinger, M.; Grin, Y. A Clathrate-I Phase with Li-Ge Framework. *Chem. − Eur. J.* **2012**, *18*, 9818−9822.
(68) Bobev, S.; Sevov, S. C. Clathrates of Group 14 with Alkali Metals: An Exploration. *J. Solid State Chem.* **2000**, *153*, 92−105.
(69) Cros, C.; Pouchard, M.; Hagenmuller, P. Sur Une Nouvelle Famille de Clathrates Mineraux Isotypes Des Hydrates de Gaz et de Liquides. Interpretation Des Resultats Obtenus. *J. Solid State Chem.* **1970**, *2*, 570−581.
(70) Kaltzoglou, A.; Hoffmann, S. D.; Fässler, T. F. Order-Disorder Phase Transition in Type-I Clathrate $Cs_8Sn_{44}\square_2$. *Eur. J. Inorg. Chem.* **2007**, 4162−4167.
(71) Zhang, Y.; Lee, P. L.; Nolas, G. S.; Wilkinson, A. P. Gallium Distribution in the Clathrates $Sr_8Ga_{16}Ge_{30}$ and $Sr_4Eu_4Ga_{16}Ge_{30}$ by Resonant Diffraction. *Appl. Phys. Lett.* **2002**, *80*, 2931−2933.
(72) San-Miguel, A.; Toulemonde, P. High-Pressure Properties of Group IV Clathrates. *High Pressure Res.* **2005**, *25*, 159−185.
(73) Kröner, R.; Peters, K.; von Schnering, H. G.; Nesper, R. Crystal Structure of the Clathrates $K_8Al_8Ge_{38}$ and $K_8Al_8Sn_{38}$. *Z. Kristallogr. − New Cryst. Struct.* **1998**, *213*, 675−676.

https://doi.org/10.1021/acsami.1c07240
ACS Appl. Mater. Interfaces 2021, 13, 42564−42578